Petroleum Science 21 (2024) 1190–1210

Contents lists available at ScienceDirect

Petroleum Science

journal homepage: www.keaipublishing.com/en/journals/petroleum-science

Original Paper

A novel responsive stabilizing Janus nanosilica as a nanoplugging agent in water-based drilling fluids for exploiting hostile shale environments

Alain Pierre Tchameni [a, b, c, d], Lv-Yan Zhuo [e], Lesly Dasilva Wandji Djouonkep [a, b, c], Robert Dery Nagre [f], Lu-Xin Chen [a, b, c], Lin Zhao [a, b, c], Chao Ma [a, b, c, **], Bin-Qiang Xie [a, b, c, *]

[a] College of Petroleum Engineering, Yangtze University, Wuhan, 430100, Hubei, China
[b] Key Laboratory of Drilling and Production Engineering for Oil and Gas, Hubei, China
[c] Lost Circulation Control Laboratory, National Engineering Laboratory for Petroleum Drilling Engineering, Yangtze University, Wuhan, 430100, Hubei, China
[d] College of Petroleum Engineering, Shandong Institute of Petroleum and Chemical Technology, Dongying, 257061, Shandong, China
[e] Petroleum Engineer Research Institute of Petrochina Dagang Oilfield, Tianjin, 300280, China
[f] Department of Chemical Engineering, Kumasi Technical University, P. O. Box 854, Kumasi, Ghana

ARTICLE INFO

Article history:
Received 4 November 2022
Received in revised form
10 October 2023
Accepted 10 October 2023
Available online 17 October 2023

Edited by Jia-Jia Fei

Keywords:
Janus nanosilica
Thermo-responsive copolymer
Anti-polyelectrolyte effect
Shale stabilizer
Inhibition
Plugging
Drilling fluid

ABSTRACT

Thermo-responsive nanocomposites have recently emerged as potential nanoplugging agents for shale stabilization in high-temperature water-based drilling fluids (WBDFs). However, their inhibitory properties have not been very effective in high-temperature drilling operations. Thermo-responsive Janus nanocomposites are expected to strongly interact with clay particles from the inward hemisphere of nanomaterials, which drive the establishment of a tighter hydrophobic membrane over the shale surface at the outward hemisphere under geothermal conditions for shale stabilization. This work combines the synergistic benefits of thermo-responsive and zwitterionic nanomaterials to synchronously enhance the chemical inhibitions and plugging performances in shale under harsh conditions. A novel thermo-responsive Janus nanosilica (TRJS) exhibiting zwitterionic character was synthesized, characterized, and assessed as shale stabilizer for WBDFs at high temperatures. Compared to pristine nanosilica (SiNP) and symmetrical thermo-responsive nanosilica (TRS), TRJS exhibited anti-polyelectrolyte behaviour, in which electrolyte ions screened the electrostatic attraction between the charged particles, potentially stabilizing nanomaterial in hostile shaly environments (i.e., up to saturated brine or API brine). Macroscopically, TRJS exhibited higher chemical inhibition than SiNP and TRS in brine, prompting a better capability to control pressure penetration. TRJS adsorbed onto the clay surface via chemisorption and hydrogen bonding, and the interactions became substantial in brine, according to the results of electrophoretic mobility, surface wettability, and X-ray diffraction. Thus, contributing to the firm trapping of TRJS into the nanopore structure of the shale, triggering the formation of a tight hydrophobic membrane over the shale surface from the outward hemisphere. The addition of TRJS into WBDF had no deleterious effect on fluid properties after hot-treatment at 190 °C, implying that TRJS could find potential use as a shale stabilizer in WBDFs in hostile environments.

1. Introduction

The world's energy need is expected to increase by nearly 50% in 2050 compared to 2010. With the current scarcity of conventional petroleum resources along with the growing need for energy, innovative research into the utilization of alternative energy sources, like unconventional resources has been explored in response to

* Corresponding author. College of Petroleum Engineering, Yangtze University, Wuhan, 430100, Hubei, China.
** Corresponding author. College of Petroleum Engineering, Yangtze University, Wuhan, 430100, Hubei, China.
E-mail addresses: 500526@yangtzeu.edu.cn (C. Ma), xbq2040@sina.com (B.-Q. Xie).

https://doi.org/10.1016/j.petsci.2023.10.008

the world's burgeoning energy needs for future generations. One of the unconventional resources of energy is shale gas. Thanks to technological breakthroughs in horizontal drilling and hydraulic fracturing, the production of shale gas in the United States has increased dramatically over the past several years (Song et al., 2013). In drilling operations, shales account for 75% of drilled formations and lead to 90% of downhole complexities including borehole collapse, cavings, tight holes, and stuck pipe (Abbas et al., 2021; Ma et al., 2019; Mehtar et al., 2010; Zhong et al., 2020). Thus, maintaining borehole stability in shale formations has become a worldwide thorny issue. In the past decades, no efforts have been spared to overcome the wellbore instability issues. Oil-based drilling fluids (OBDFs) have been preferentially adopted as the best possible option to drill most water-sensitive shale formations due to minimal oil/shale interactions (Geng et al., 2021; You et al., 2014). However, the high cost and stringent environmental regulations worldwide restrict their wide applications (Caenn and Chillingar, 1996). Albeit attempts have been made to use synthetic-based drilling fluids (SBDFs) with low-deleterious environmental impacts while preserving the technical operating performance comparable to that of OBDFs (Li et al., 2016a, b), these fluids were still expensive (Caenn and Chillingar, 1996; Friedheim, 1997). At the same time, environmental, maintenance, and cost considerations have resulted in the increasing adoption of water-based drilling fluids (WBDFs), and their applications account for approximately 80% of all wells (Lei et al., 2021).

As shale is mainly composed of mineral clays, it is susceptible to hydration and dispersion effects when it encounters traditional WBDFs during drilling operations. This leads to complex physical and chemical interactions such as loss of hydraulic overbalance, changes in swelling pressure, and alteration of shale water content (Ge et al., 2015; Kang et al., 2017). To alleviate these issues, physical plugging of pores and micro-fractures from water influx in shale has been adopted as the best possible approach to sustain wellbore stability. However, the commonly used plugging agents, including ultra-fine calcium carbonate, graphite, and elastic particles (i.e., cross-linked polymer) are micro-sized particles, which are larger than the nanopores of shale formations (Lv et al., 2017; Ma et al., 2019; Zhong et al., 2020). Besides, because of their non-ideal physical plug, they fail to form an effective plugging membrane, resulting in inexorable water ingress into the shale, which ultimately compromises the stability of the formation during drilling operations (Huang et al., 2021a; Koteeswaran et al., 2017; van Oort, 1997; Parvizi Ghaleh et al., 2020). Therefore, controlling the pore pressure penetration in the formation and shale swelling/dispersion inhibition properties is key to strategically sustaining the stability of shale formation.

Zwitterionic materials (species with an overall neutral charge but covalently linked cationic and anionic groups) have piqued the interest of researchers due to their ability to be adsorbed onto the surface of clay particles (i.e., strong interaction between the charged groups of the zwitterionic materials and the oppositely charged sites of clay platelets through chemisorption), thereby significantly inhibiting shale swelling and dispersion properties (Du et al., 2020; Ren et al., 2021; Xie et al., 2016). Du et al. (2019, 2020) recently reported a series of low molecular weight zwitterionic copolymers that could perfectly mitigate shale hydration and dispersion as they could penetrate into the interlayer spacing of clay and modify the internal micro-structure. Moreover, zwitterionic materials exhibit a special salt-responsive behaviour in which the copolymer shell adopts a collapsed conformation in water due to potent electrostatic attractive forces (including charge-charge, charge-dipole, and dipole-dipole interactions) between the ionic groups (Xiao et al., 2018b). Benefiting from the pseudo “anti-polyelectrolyte effect,” the zwitterionic species increase the excluded volume in brine because the counter ions would screen the electrostatic attractive energy, which would minimize the net dipole moments and subsequently increase the colloidal stability of nanomaterials (Sun et al., 2020). Contrarily, the well-known polyelectrolyte effect contributes to copolymer shell shrinkage in the presence of electrolyte ions because the counter ions shield the electrostatic repulsion and, as a result, gradually destabilize the colloidal stability of nanomaterials (Sun et al., 2020). From an intuitive viewpoint of engineerable chemical structures of zwitterionic species, the variation of cationic and anionic pairs. The key functional groups, including ammonium, imidazolium, and pyridinium, which correspond to carboxylate, sulfonate, and phosphate, respectively, can be used to create various zwitterionic species with tuned and optimized inter- and intra-molecular interactions among the charged groups in brine (Xiao et al., 2018a).

In recent years, the advent of nanotechnology has stimulated great interest in the petroleum industry, and considerable research has been devoted to the applicability of nanomaterials as shale stabilizers in WBDFs (Huang et al., 2021b; Naji et al., 2021). A variety of nanomaterials, such as silica, graphene oxide, carbon nanotubes, and polymer latex, were first employed as promising shale stabilizers in WBDFs (Barry et al., 2015; Liu et al., 2019; Xu et al., 2018). However, as the underground environments are very complex and characterized by a maximum salinity concentration and temperature of 31.7 wt% and 150 °C, respectively, the agglomeration of nanomaterials was the common denominator of all issues (Ma et al., 2019; Ranka et al., 2015). Numerous reports showed that high ionic strength significantly contributes to nanomaterial flocculation, largely because of the charge screening effect, while high temperatures disrupt the collision probability resulting in a reduced surface area-to-volume ratio of the nanomaterials and thus giving rise to flocculation (Yeap, 2018). The preceding unwanted phenomenon, therefore, limits the applicability of nanomaterials as shale stabilizers under complex downhole conditions.

As changes in external environmental stimuli are involved in various processes in petroleum industries, responsive materials have been intensively studied over the years (Xu et al., 2022; Ma et al., 2019; Tchameni et al., 2021a; Xie et al., 2021; Li et al., 2017; Wang et al., 2015; Bai et al., 2022; Shen et al., 2022; Wang et al., 2017). Responsive materials undergo a timely irreversible or reversible phase transition in solution by responding to environmental changes (i.e., temperature, salinities, and pH) in particularly showing Lower Critical Solution Temperature (LCST), which affects a change microstructure and physico-chemical properties (Rivera-Tarazona et al., 2021). Contrary to the behaviour of responsive materials, conventional materials can also undergo changes in microstructure, physical and chemical properties but do not exhibit LCST behaviour in solution upon external environmental conditions. Among the responsive materials, the thermal responsive ones have been tremendously researched for diverse applications in petroleum industries especially in drilling fluids (Xie et al., 2021; Tchameni et al., 2021b), enhanced oil recovery (Li et al., 2017), and fracturing fluid (Li et al., 2019a, b; Cao et al., 2021). Because of the unique property of these materials, a strong tendency in combining thermo-responsive materials and nanoparticles to develop nanocomposites with enhanced shale plugging performances have recently been the research hotspot (Bai et al., 2022; Shen et al., 2022; Wang et al., 2015, 2017). Albeit auspicious results were obtained, there are still some inadequacies to be addressed for effectively preserving the stability of the shale during drilling operations. Table 1 lists some works focusing on the thermo-responsive materials used as shale stabilizers in WBDFs.

For most shale stabilizers, their chemical inhibition was solely demonstrated by the wettability test, which does not substantially reflect the inhibitory effect (shale swelling/dispersion inhibition

Table 1
Some investigated thermo-responsive materials as shale plugging in WBDFs.

Molecular structure	Test conditions	Properties investigated	Advantages	Disadvantages	References
SiO_2-g-poly(NIPAm-*co*-AMPS) (Amino-based-SiO_2) (NPA)	From room temperature to 150 °C	Plugging performance (room temperature to 80 °C), chemical inhibition compatibility tests (rheological and filtration loss properties at 150 °C)	NPA having a median particle size of 190 nm could not only reduce the core permeability to 0.031×10^{-7} μm^2, but also the core surface wetting angle increased from 27.18° to 77.22°. NPA also showed good compatibility in drilling fluid	The chemical inhibition was only demonstrated by wettability test.	Shen et al. (2022)
SiO_2-g-poly(NIPAm-*co*-AMPS) (Vinyl-terminated-SiO_2)	From room temperature to 130 °C	Chemical inhibition (wettability test) compatibility tests (rheological and filtration loss properties at 130 °C)	The plugging agent having a particle size of 49.665 μm increased the contact angle from 20° to 108°	The plugging performance was only studied by F_{API} and F_{HTHP}. The chemical inhibition was only demonstrated by wettability test.	Bai et al. (2022)
Poly(MMA-*co*-St)-*g*-poly(NIPAm-*co*-AA) (SD-SEAL)	From room temperature to 180 °C	Plugging performance from room temperature to 180 °C and chemical inhibition	SD-SEAL having an average particle size of 100 nm could reduce the core permeability to 0.048×10^{-7} μm^2 and the core	The core permeability was not reported. The chemical inhibition was only demonstrated by wettability test.	Wang et al. (2017)
SiO_2-g-poly(NIPAm-*co*-AA) (Vinyl-terminated-SiO_2)	From room temperature to 150 °C	Plugging performance from room temperature to 150 °C and chemical inhibition	The plugging agent having a particle size of 15 nm could reduce the pore pressure penetration. Moreover, the core surface wetting angle increased from 0° to 120°.	The chemical inhibition was only demonstrated by wettability test.	Wang et al. (2015)

performance) of these materials. Having in mind that, as the surface wettability of thermo-responsive shale stabilizer evenly changed from hydrophilicity to hydrophobicity above the lower critical solution temperature (LCST) (Tchameni et al., 2020b), a weak interaction between the plugging agents and the hydrophilic surface of shale might be expected. As a result, the establishment of a tight hydrophobic membrane over the shale surface to efficiently mitigate water intrusion in shale formation could be compromised. Consequently, lower intercalation into the interlayer confinement of clay particles to expel free water could not be excluded under certain conditions (Lv et al., 2020). Therefore, hunting for an effective shale stabilizer in WBDFs for optimal shale exploitation is a matter of urgency.

In the past, the "Janus nanoparticles" was conceptualized by De Gennes (1992). The name "Janus" refers to a special class of particles having two faces looking in opposite directions to describe the distinct chemistry and physics on their two hemispheres. Because of structural characteristics, Janus nanoparticles afford the possibility to achieve diverse and synergistic functionalities. With a continuous depletion of conventional petroleum resources, the exploitation of shale resources even under vigorous downhole conditions is expected to balance the growing need for energy. With this in mind, a sophisticated approach to maximize the advantageous characteristics of a thermo-responsive shale stabilizer is urgently needed. If thermo-responsive shale stabilizer could exhibit zwitterionic character by possessing negatively charged and positively charged at the two hemispheres, respectively, the colloidal stability of the material would be improved in brine attributed to the anti-polyelectrolyte effect in brine as illustrated in Fig. 1.

Benefiting from the anti-polyelectrolyte effect, the key functional groups of the zwitterionic materials are shielded by salts, allowing molecular chains to stretch and ultimate stability in brine. Therefore, the thermo-responsive Janus nanocomposite endowed with this property would not only be stabilized but also exhibit a certain LCST behaviour in brine. As a result, the positively charged groups in the inward hemisphere of Janus nanocomposite would strongly interact with the negatively charged site of clay particles to consolidate the hydrophobic membrane of the outward hemisphere over the shale surface for effective synergy. Thus, this would promote the establishment of a tighter hydrophobic membrane at the outward hemisphere resulting in effective shale/water interactions, which would greatly enhance the stability of the shale formation under challenging geothermal conditions.

In this work, a novel strong inhibitive nanocomposite (TRJS), nanosilica was grafted with amine functional groups on the inward hemisphere and poly(acrylic acid-*co*-N-vinyl caprolactam) on the outward hemisphere via surface-initiated atom transfer radical polymerization (SI-ATRP) to achieve a high grafting density (Ma et al., 2019). The developed TRJS exhibited favourable colloidal stability under hostile environmental conditions, which beneficially improved the stability of the shale formation during drilling operations. Under high geothermal conditions, TRJS could simultaneously oppose pore pressure penetration in the formation by reducing the shale permeability and chemically inhibiting the shale hydration and dispersion. To the best of the author's knowledge, the study of thermo-responsive Janus nanocomposite exhibiting zwitterionic character for application in WBDFs as shale stabilizers under vigorous conditions has no historical precedent in the published literature.

2. Experimental

2.1. Materials

Nanosilica (φ = 50±5 nm, 99.5%), N-β-(Aminoethyl)-γ-aminopropyl trimethoxy silane (AEAPTS, 95%), N-Vinylcaprolactam (NVCL, 99%), acrylic acid (AA, >98%) were acquired from Shanghai Macklin Biomedical Co. Ltd. Paraffin wax (with a melting point between 62 and 64 °C), 2,2-azobis (2-methylpropionamide) dihydrochloride (AIBI, 98%) were acquired from Shanghai Acmec Biochemical Co. Ltd. Copper (I) bromide (Cu (I) Br, 99%), 2-bromoisobutyryl bromide (2-BIBB, 97%), N, N, N, N, N″-pentamethyldiethylenetriamin (PMDETA, 99%), dimethylformamide (DMF, 99%), and trimethylamine (TEA, 98%) were bought from Shanghai Bidepharmtech Co. Ltd. Ethanol (EtOH, 99.5%), sodium hydroxide

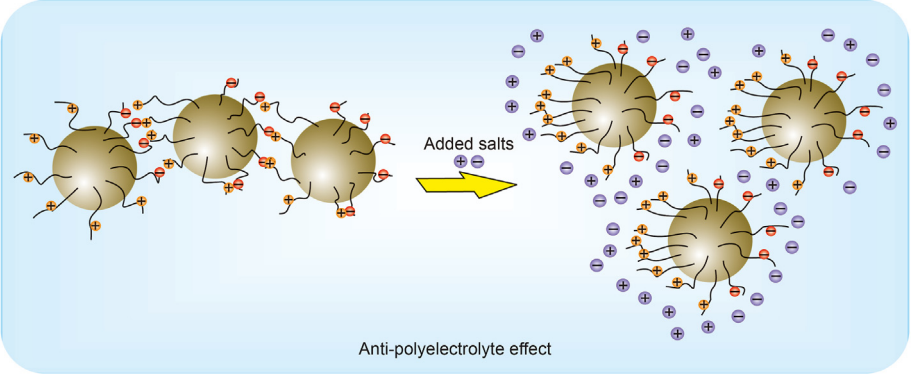

Fig. 1. Schematic representation of the anti-polyelectrolyte effect.

(NaOH, 96 %), sodium chloride (NaCl, 99.5%) and calcium chloride ($CaCl_2$, 98%) were from Tianjin Beilian Fine Chemicals Development Co. Ltd. All the chemicals in this research were used as received without additional purification. The electric heating water distiller (Biobase Meihua Trading, Model WD-A20) was used for water distillation. The sodium bentonite provided by Jingzhou Jiahua Technology Ltd. was according to the API standard. The sodium montmorillonite (Na-Mt) used for zeta potential analysis, FT-IR, and XRD were purchased from Shanghai Bidepharmtech Co. Ltd. The shale-drilled cuttings used for the hot-rolling dispersion test were acquired from China National Petroleum Corporation (CNPC) Western Drilling Engineering Co., Ltd. (Karamay, China). The mineralogical composition of the shale-drilled cuttings is listed in Table 2.

2.2. Synthesis of thermo-responsive Janus nanosilica (TRJS)

The synthesis of TRJS was carried out in distinct steps as summarized in Scheme 1.

2.2.1. Amino-functionalized nanosilica/wax beads

Initially, nanosilica was functionally treated with amino groups. In brief, dried nanosilica (4 g) was dispersed under intense ultrasonication in ethanol (100 mL) at room temperature. Subsequently, 2 g of AEAPTS, previously dissolved in EtOH, was added dropwise to a colloidal nanosilica solution. The functionalization reaction was performed at ambient temperature for 24 h. The amino-modified nanosilica was recovered by centrifugation (4000 rpm for 30 min at ambient temperature) after several washing procedures with EtOH to remove the unreacted coupling agents. The product was purified several times until the supernatant tested negative for amines (observation of slightly yellow coloration after adding ~10 mg of ninhydrin and heated at 65 °C for 0.5 h) (Soto-Cantu, 2008). Afterward, dried amino-functional nanosilica was homogeneously dispersed in melted paraffin wax under mechanical stirring, and boiling water (pH = 8) was added to the flask under constant stirring with a half-moon stirrer at 1500 rpm for 1 h at 80 °C. Then the emulsion formed was cooled to ambient temperature, repeatedly washed, and filtered using distilled water, then EtOH, and finally dried under ambient temperature (Hong et al., 2006).

2.2.2. NH_2–SiO_2@PAA@PNVCL Janus nanosilica (TRJS)

Approximately 10 g of colloidosomes were dissolved in 250 mL of dry DMF (dried three times over 4 Å molecular sieves) containing 3 mL of TEA under constant stirring in a three-necked flask under nitrogen atmosphere with the reaction temperature-adjusted to 0 °C in an ice bath. Subsequently, 5 mL of BIBB was introduced into the above mixture under continuous stirring. Once the addition was completed, the reaction was conducted at ambient temperature for 15 h under a nitrogen atmosphere. Afterward, modified colloidosomes were collected by vacuum filtration and exhaustively washed with distilled water to remove unattached particles. Then, the achieved wax/modified nanosilica beads were dried at room temperature overnight. Next, the dried product was dissolved in hot chloroform to eliminate traces of paraffin wax. The resultant product was redispersed in EtOH, followed by repeated centrifugation and purification in DMF to obtain the purified NH_2–SiNP–Br. PAA@PNVCL was anchored on the macro-initiator as follows; NH_2-SiNP-Br were ultrasonically dispersed in the mixed solvents consisting of 30 mL distilled water and 20 mL of DMF for 30 min, then AA (1.70 g, 23.60 mmol) with a pH adjusted to 8, NVCL (3.30 g, 23.70 mmol), PMDETA (0.0875 g, 0.05 mmol), and Cu(I)Br (0.037 g, 0.025 mmol) were poured in a three-necked flask equipped with a rubber septum, degassed and charged with N_2 atmosphere. The polymerization was performed under stirring at 60 °C for 240 min. After the polymerization, the resulting Janus nanocomposite was purified via multiple centrifugation procedures.

2.3. Structural characterization

Fourier transform infrared spectroscopy instrument FT-IR 650 (Tianjin, China) and the thermogravimetric analysis (TGA) was carried out on a Pyris 1 thermogravimetric analyzer with a heating rate of 10 °C/min from 30 to 900 °C under a nitrogen flow of 50 mL/min. The microscopic morphologies of nanoparticles and shale were observed using JEOL 7400 FEG-SEM Scanning Electron Microscope (SEM). The molecular weight (M_w) and molecular distribution (*PDI*) of grafted PAA@PNVCL chains acquired were before treatment of the nanocomposites with hydrofluoric acid (HF) to cleave to the grafted polymer and unattached films. Subsequently, gel permeation chromatography (GPC) was done at 35 °C on a Waters GPC with THF as the eluent. The electrophoretic mobilities

Table 2
Mineralogical composition of the shale samples.

Component	Quartz	Potassium feldspath	Plagioclase	Calcite	Dolomite	Augite	Clay mineral
Content, wt%	31.3	1.3	2.4	17.8	2.3	2.5	42.4

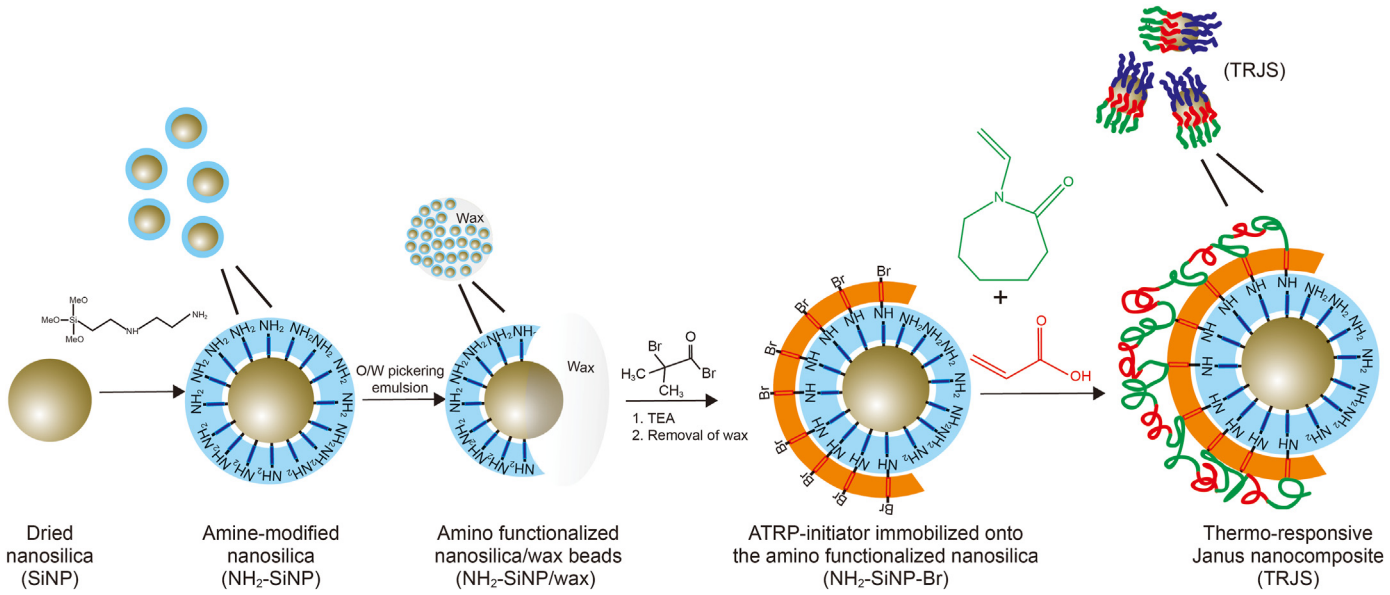

Scheme 1. Synthetic route to prepare TRJS.

(EPM) and TEM analyses were conducted before the dispersion of 0.2 g of nanocomposites in 100 mL by intensive ultrasonication at ambient temperature for 30 min. Afterward, the droplets were passed through a copper grid coated with a carbon film and air-dried for TEM examination. TEM analysis was carried out using JEM-2100UHR, JEOL, Japan. Malvern Instruments Zetasizer Nano Z was used to examine the EPM of the samples.

2.4. Responsivity analysis

About 3 mL of the above-prepared dispersion was introduced into a dried cuvette glass for measuring the transmittance using a 721-type UV–vis Spectrophotometer at 500 nm (Shanghai Xianke Instrument, China). The temperature at which the transmittance obviously reduces with rising temperature was assimilated to the LCST of samples. This technique was extensively employed to detect the LCST of thermo-responsive materials in the literature (Durand and Hourdet, 1999; Guo et al., 2015; Xie et al., 2019).

2.5. Colloidal stability

The colloidal stability of nanoparticles is vital to maintain their desirable characteristics as aggregation which often drives performance exhaustion in drilling fluids under hostile conditions. Into 10 mL of nanosilica, the dispersion was added 90 mL of brine concentrated at 5, 10, 15, 20, 25, and 30 wt/v%, and American Petroleum Institute (API) brine (8 wt/v% NaCl+2 wt/v% $CaCl_2$) which constituted 9:1 vol ratio (Zuniga et al., 2016). The mixtures contained in glass bottles were ultrasonically dispersed for 15 min at room temperature and then heated at the desired temperature over time, chilled to room temperature, and colloidal stability was inspected by visual observation. The extent of particles settling at the bottom of the glass after the intervals of 10, 20, and 30 days were used as a criterion for the stability of the dispersion (the more the particle settling, the higher the instability of dispersion) (OECD, 2017). Besides, aliquots (~5 mL) were collected for monitoring the variation in particle size on a particle size analyzer (BT-9300LD, Betttersize, Shanghai, China).

2.6. Shale stabilization properties

2.6.1. Linear swelling test and drilled shale hot-rolling recovery test

Na-Mt pellets were prepared by first crushing the shale samples to a fine powder (<100 mesh), followed by pressing approximately 10 g of the Na-Mt powder samples at 10 MPa for 600 s. The initial thickness (H_o) of each Na-Mt pellets sample was taken. Afterward, the Na-Mt pellets were placed in an HTHP dilatometer (Tuochuang, China), and the linear swelling rate over 16 h was investigated after the Na-Mt pellets interacted with 10 mL of testing fluids without salts and with salts (4% wt/v% NaCl) containing distinctive samples of nanocomposites. Then the linear swelling rates were calculated via the following equation;

$$D = \frac{R_t - R_i}{H_o} \times 100\% \quad (1)$$

where D represents the linear swelling rate; H_o represents the initial thickness in mm; R_i represents the initial reading in mm; R_t is the reading after the appointed time t.

The inhibitive effect of the testing fluids was examined by a shale-drilled hot-rolling dispersion test. This test was designed to check the ability of the testing fluids (without salt and in the presence of 4 wt/v%) to suppress shale hydration and dispersion under geothermal conditions. Into 350 mL of the above-prepared testing fluids contained in the sealable cell, was added 50 g of shale cuttings, and hot-rolled at the desired temperature for 16 h. Afterward, the residual shale cuttings in cells were sieved through a 40-mesh, rinsed with water, and dried at 105 °C for 6 h, the shale recovery rate was calculated using the following relationship (Li et al., 2019a, b);

$$R = \frac{W_2}{50} \times 100\% \quad (2)$$

where W_2 is the weight of shale cuttings recovered after hot oven-treatment.

2.6.2. Pore pressure transmission experiment

The pore pressure transmission experiment was designed to assess the plugging performance of the prepared fluid samples using a pressure transmission experimental setup made by Tuochuang Scientific Instrument, China (Song et al., 2013; Xu et al., 2017; Zhong et al., 2020). The experimental setup and schematic diagram of the pressure transmission experiment are shown in Fig. 2.

The shale cores samples from the Longmaxi Formation were initially vacuum-treated, and saturated with 4 wt/v% NaCl and installed in a shale core holder with a confining pressure maintained at 5 MPa. The upstream and downstream pressure lines were set to constant values of 2.0 and 1.0 MPa, respectively, while the shale cores were heated to formation temperature. The differential pressure between the upstream line and downstream line was mainly responsible for the pressure transmission in the shale core. When attaining the pressure balance, the brine in the upstream chamber was replaced with the plugging fluids (constituted of 4 wt/v% NaCl brine and 0.2 wt/v% TRJS or TRS), with the pressures at both upstream and downstream line maintained at 2.0 and 1.0 MPa, respectively. During the entire experimental process, the downstream pressure line was maintained, and its equilibrium indicated the plugging ability of samples. The permeability of the shale samples was calculated using the following relationship (Xu et al., 2017).

$$K = \frac{\mu\beta VL \ln\left(\frac{P_m - P_o}{P_m - P(L,t_2)}\right) - \ln\left(\frac{P_m - P_o}{P_m - P(L,t_1)}\right)}{A(t_2 - t_1)} \quad (3)$$

where K represents the permeability of the shale core samples in μm^2; μ represents the viscosity of testing fluids in mPa·s; β represents the static compression ratio of testing fluids in MPa^{-1}; V represents the enclosed volume of the testing fluids in the downstream in cm^3; A represents the cross-section area of the shale core samples in cm^2; L represents the length of shale core samples in cm; t represents the overall experimental time in s; P_m represents the upstream pressure in MPa; P_o represents the pore pressure in MPa; and finally $P(L,t)$ represents the real-time downstream pressure in MPa.

The compression ratio of testing fluids is given as follows: $\beta = -\frac{\Delta V/V}{\Delta P}$, where $\frac{\Delta V}{V}$ represents the relative reduction in the volume of fluid (dimensionless); and ΔP represents the relative change in pressure in MPa.

After the experimental process, the corresponding end face of the shale core samples that interacted with the testing fluids were cut, dried in a vacuo, and the surface micro-morphology was observed by a Zeiss Gemini SEM-HRSEM.

2.7. Interaction between modified nanosilica and clay particles

2.7.1. Electrophoretic mobility (EPM) analysis

Malvern Instruments Zetasizer Nano Z was used to examine the impact of pH value on EPM of nanocomposites. Besides, the effect of pH on EPM of Na-Mt and Na-Mt/nanocomposites systems was also investigated. The concentration of the sample was fixed at 0.1 wt/v %, and the pH of the mixtures was adjusted using 1 N HCl and 1 N NaOH in distilled water and brine (4 wt/v%) at room temperature.

2.7.2. Surface wettability and interlayer spacing measurements

The surface wettability of the above-prepared shale pellets was studied by taking the contact angle between the shale surface and nanocomposites dispersions [in distilled water or brine (4 wt/v%)]. A contact angle goniometer (JC2000D5M, Zhongchen, China) was used to examine the wettability of the surface of the pellets (Lv et al., 2020). Additionally, the interactions between the nanocomposites (TRJS and TRS) and Na-Mt were also studied by XRD. Into the above-prepared Na-Mt suspension [in distilled water or brine (4 wt/v%)], was added 0.01 g of nanocomposites, followed by intensive ultrasonication and stirring for a day at room temperature to ensure effective dispersion. The mixtures obtained were centrifuged and washed at least thrice to remove unabsorbed nanocomposites. After the purification, the wet-precipitate was used for X-ray diffraction (XRD) analysis (X'Pert PRO MPD diffractometer from Analytical B.V., Amsterdam, Holland) to examine the variation in interlayer spacing at distinct temperatures (Lv et al., 2020).

2.7.3. Isothermal adsorption

The adsorption isotherm test was carried out to elucidate the adsorption mechanism. Na-Mt (0.1 g) was added into a measured volume of nanocomposite solution (Co). The adsorption test was conducted by first stirring the mixture at high-speed, then allowing it to stand for 0.5 h for the adsorption process at the desired temperatures. Afterward, the mixture was centrifuged and the

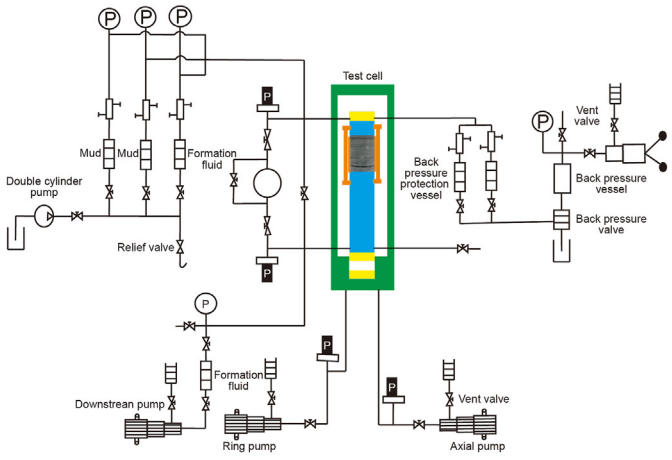

Fig. 2. Experimental setup and schematic diagram used for pore transmission test.

concentration of un-absorbed nanocomposites (C_1) that remained in the supernatant was determined using an ultraviolet spectrophotometer (V-1300 Macy Instrument, China) with scanning wavelengths between 320 and 400 nm (Tchameni et al., 2020a). The quantity of nanocomposites adsorbed onto the Na-Mt surface was calculated using the following equation;

$$M = \frac{(C_o - C_1) \times V}{m} \quad (4)$$

where M is the weight of adsorbed nanocomposites per unit weight of Na-Mt in mg/g; C_o and C_1 are the nanocomposites concentration before and after the adsorption onto Na-Mt surface in mg/L; V is the volume of solution in L; m is the weight of Na-Mt used in g.

2.8. Compatibility test

A fixed concentration of nanocomposites was dispersed in the base fluid (BF), which was composed of 4 wt/v% pre-hydrated clay slurry (bentonite:attapulgite=1:1)+0.5 wt/v% VIS-H+5 wt/v% SMP-3+5% wt/v% SPNH+3 wt/v% $CaCO_3$+3% wt/v% lubricant+4 wt/v% NaCl+0.5 wt/v% Na_2SO_3+barite (ρ = 2.0 g/cm^3). It was worth noting that, the attapulgite clay was added to reduce the high-yield stress attributed to bentonite flocculation after the hot rolling process (Zhang et al., 2017; Altum and Serpen, 2005). The fluid samples were prepared under mechanical stirring at 10000 rpm using a high-speed blender. After the heat-treatment process at a temperature of 190 °C for 16 h in a roller oven (OFI Testing Equipment, US), the fundamental properties of the fluids samples including rheological, and filtration properties, and density were examined. The compatibility of nanocomposite in WBDFs was studied by comparing the above-mentioned properties of the fluid-bearing nanocomposite and base fluid.

The typical procedure to examine the rheological characteristic involved cooling the hot-rolled fluid samples to ambient temperature, followed by uniform stirring in a mixing cup prior to the measurement by ZNN-D6B six-speed rotational viscometer (Qingdao Shande Petroleum Instrument, China). The data were taken at ambient temperature and the rheological parameters using the following formulae as prescribed by the API standard procedure for field-testing of drilling fluids (Xiong et al., 2014).

$$\text{Apparent viscosity } (AV) = 0.5 \times \theta_{600} \text{ (mPa·s)} \quad (5)$$

$$\text{Plastic viscosity } (PV) = \theta_{600} - \theta_{300} \text{ (mPa·s)} \quad (6)$$

$$\text{Yield point } (YP) = 0.5 \times (\theta_{300} - PV) \text{ (Pa)} \quad (7)$$

3. Results and discussion

3.1. Synthesis of TRJS

Scheme 1 presents a schematic description of the synthesis route of TRJS. Amino-modified nanosilica (NH_2-SiNP) was first prepared by reacting pristine nanosilica (SiNP) with AEAPTS, followed by Pickering emulsion masking resulting in the formation of wax colloidosomes, that is, the wax droplets decorated with SiNP as indicated in Fig. 3(a). The magnified surface of wax colloidosomes shown in Fig. 3(b) clearly revealed the exposed opposite hemisphere, which affords further chemical modification of the surface of the particles. PAA@PNVCL was finally anchored on an exposed amino-grafted hemisphere via SI-ATRP to produce TRJS. The TEM micro-photograph in Fig. 3(c) indicates that the particles were uniformly spherical with nano-scale diameters, ranging from 70 to 190 nm and the average particle size was 110.15 nm. Moreover, from the same figure, it was seen that the copolymer indicated by the arrow covered approximately 1/5 of the surface area of the SiNP particle. A control experiment using aqueous solution of symmetrical nanocomposite, TRS (average particle size of 169.5 nm in the range of 85–195 nm) for TEM imaging was also carried out to further illustrate the Janus nature of TRJS, and the results indicated in Fig. 3(d) depicted the complete absence of the asymmetrical feature previously observed.

3.2. Molecular characterization

The FT-IR spectrum of nanosilica and modified nanosilica are represented in Fig. 4. The asymmetric stretching of Si–O–Si contributed to the peaks at 803.20 and 1135.38 cm^{-1}. The vibrations of SiO–H and O–H were observed at 1643.53 and 3458.22 cm^{-1}, respectively as indicated in Fig. 4(a). The reaction of nanosilica and AEAPTS afforded the peaks at 2903.70 and 1485.77 cm^{-1} attributed to the stretching vibration of CH_2– and bending vibration N–H in AEAPTS, respectively (Fig. 4(b)). The preceding findings prove the successful anchoring of AEAPTS onto the surface of nanosilica by chemical bonding. From Fig. 4(c), the new adsorption peaks between 2929.34–2846.90 cm^{-1} for CH_2– and CH–, 1534.57 cm^{-1} for –CONH which are characteristic adsorption peaks of ATRP initiator (BIBB), revealed the successful immobilization of BIBB onto the surface of nanosilica. Thus, forming a macromolecular initiator (NH_2-SiNP-Br) with a terminal alkyl bromide onto one hemisphere from where the polymer chain growth would be initiated via SI-ATRP. From Fig. 4(d), it can be noticed that, in addition to the new adsorption peak detected at 1780.56 cm^{-1}, which was due to stretching of $-COO^-$ from AA, the characteristics of related to CH_2– and CH– and –CONH increased due to the copolymerization with NVCL and AA. Contrary to Fig. 4(d), the adsorption characteristic peaks of N–H bending vibration at 1485.77 cm^{-1} in Fig. 4(e) disappeared, which proved the Janus geometry of TRJS.

The TGA analyses of SiNP and modified SiNP are shown in Fig. 5 and the residual weight in organic matter was examined to reflect their thermo-stability. The residual weight of SiNP at 1000 °C was ~92.11 wt%, which was higher than NH_2-SiNP (90.03 wt%) attributed to the elimination of AEAPTS. The substantial decrease in residual weight of about 87.13 wt% for NH_2-SiNP-Br originated from the elimination of BIBB, where the quantity of initiator anchored onto the surface of NH_2-SiNP was estimated as 3.10 wt%. The residual weight of the copolymer was obtained as 69.82 wt% from which was calculated the copolymer weight content of 17.31 wt%. Similarly, the weight content of the initiator and copolymer for symmetric nanocomposite (SiNP-PAA@PNVCL) were obtained as 6.25 and 39.25 wt%, respectively. These findings indicate the deposition of PAA@PNVCL onto the nanosilica surface. However, the copolymer amount of TRS was higher than TRJS due to the much more initiating site on symmetric TRS nanocomposites.

The M_w and PDI of the cleaved grafted chain on TRJS were 2123 g/mol and 1.73, respectively, whereas that of TRS were 2354 g/mol and 1.82. These values indicated that TRS had a slightly higher grafting polymer density with broader molecular weight distribution than TRJS.

3.3. Responsivity analysis

To understand the effect of anisotropy of Janus geometry nanoscale materials on thermo-responsivity, a comparative study between the TRJS solution and TRS solution was carried out by tracking the turbidity of the solutions. In this experiment, the temperature-dependence optical transmittance of nanocomposite

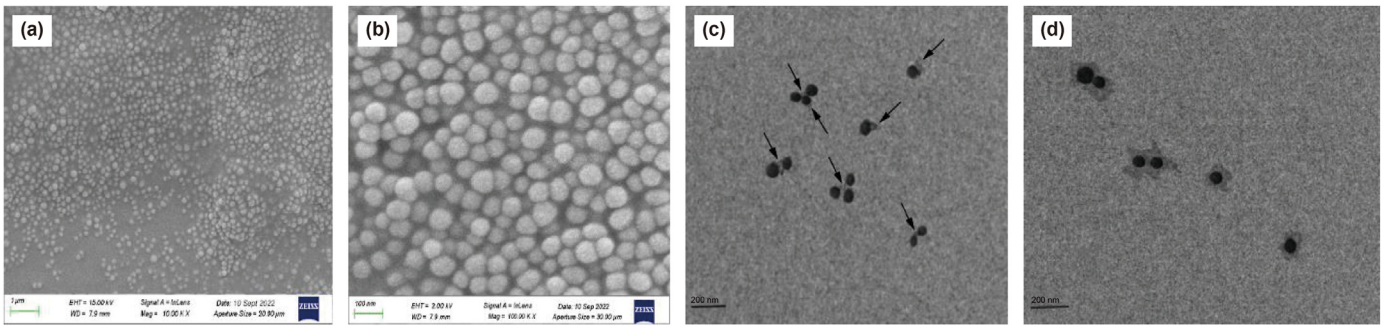

Fig. 3. (**a**) SEM micro-photographs of colloidosomes coated with NH_2-SiNP; (**b**) SEM of the magnified surface of colloidosomes indicating packing of NH_2-SiNP; (**c**) TEM micro-photographs of diluted TRJS with the arrows indicating the partially coating of SiNP surface with copolymer; (**d**)TEM micro-photographs of diluted TRS with the surface entirely covered with copolymer.

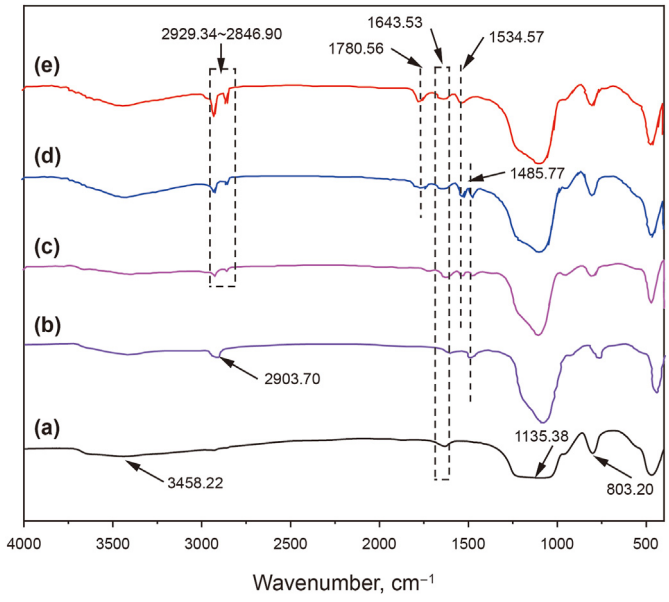

Fig. 4. FT-IR spectra of pristine nanosilica and nanocomposites; (**a**) SiNP, (**b**) NH_2-SiNP, (**c**) NH_2-SiNP-Br, (**d**) TRJS, and (**e**) TRS.

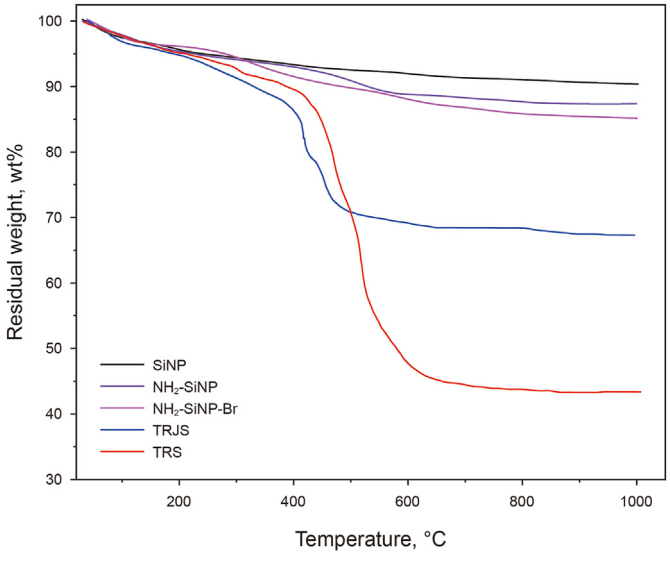

Fig. 5. TGA curves of pristine nanosilica and nanocomposites.

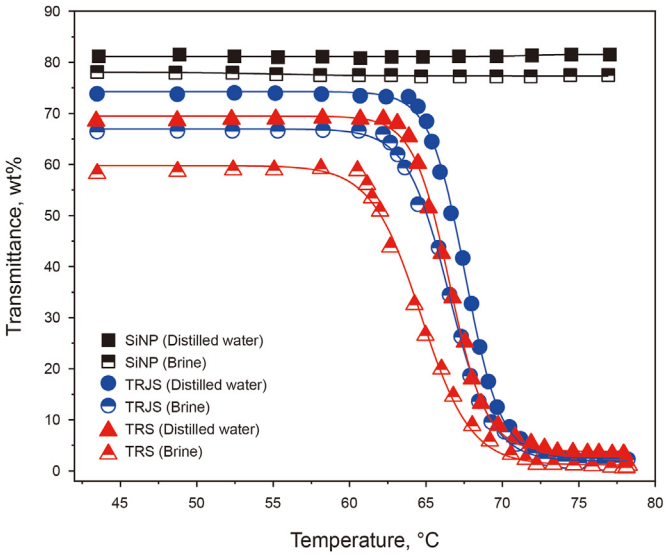

Fig. 6. Optical transmittance of pristine nanosilica and nanocomposites as a function of temperature (C_p = 0.2 wt/v%).

solutions was monitored upon warming. As indicated in Fig. 6, the transmittance of SiNP was constant throughout the temperature, which is expected for nanosilica. Conversely, the optical transmittance reduced with rising temperature, which reflected the thermo-responsiveness of TRJS and TRS. At ambient temperature, the original transmittance of nanocomposites was 72.56% and 65.23% for TRJS and TRS, respectively. When testing at the same concentration, TRJS was less slightly transparent than TRS, which was largely attributed to the formation of hydrogen bonds between the amino groups and surrounding water molecules at low temperatures, increasing the hydrophilicity of TRJS, and eventually a slightly higher phase transition temperature (Djouonkep et al., 2023). The phase transition temperature of TRJS and TRS were 64 and 65.5 °C, respectively. Thus, the phase transition in TRJS occurred at 1.5 °C higher than that of TRS. This phenomenon indicated that the phase transition of nanocomposite aqueous solutions was essentially controlled by hydrogen bonding and hydrophobic effect, which was consistent with the previous work (Li et al., 2021). Below the LCST, the polar groups (−CONH of NVCL and $-COO^-$ of AA) in the outward hemisphere of the particle imbued the nanocomposite with hydrophilicity. Thus, they could solvate the copolymer shield by interacting with the neighbouring water molecules through hydrogen bonds. It has been reported that a thermo-responsive material is soluble and transparent in the water

below the LCST (Akimoto et al., 2014). Above the LCST, it is speculated that as VCL thermo-responsive subunits exhibit a more hydrophobic character, the thermal motion of the polymer chains upon heating triggers the breakage of hydrogen bonds between the polar groups in the thermo-responsive hemisphere. This mitigated the interaction between the polymer film and water molecules, and ultimately a reduction of optical property. However, TRJS exhibited extra hydrophilicity at high temperatures, presumably ascribed to amino functional groups in the inward hemisphere, which could be the reason why the phase transition rose toward higher temperatures. In brine, the transmittance of nanomaterials declined, especially for TRS and TRJS, by almost 8.32% and 4.16%, respectively, attributed to the "salting-out" effect in poor solvent quality, causing a decrease in the hydration state of LCST chains, and eventually the self-assembly of LCST chains (Guo et al., 2015). Simultaneously, the LCST of TRS and TRJS diminished to 59 and 63.5 °C, respectively. The polyelectrolyte effect (as explained in the introduction) in TRS presumably contributed to its significant hydrophobic association characteristic, whereas TRJS is governed by the anti-polyelectrolyte effect (as explained in the introduction) as counter ions penetrate into the nanocomposite molecular chains and prevent the electrostatic inter/intrachain dipole–dipole interaction. Subsequently, a reduced chain-chain interactions contributed to a certain hydrophilic groups-water interactions, which minimized the extent of the hydrophobic associative phenomenon in brine (Xiao et al., 2018a).

3.4. Colloidal stability

The stability of unmodified nanosilica and modified nanosilica was investigated in brine and standard API brine. Preliminary results on stability testing showed that the unmodified nanosilica in brine (NaCl 10 wt/v%) and API brine underwent precipitation after settling for 2 h, which was indicative of its high instability under the investigated conditions, and the mean particle size was detected as 2.235 μm. Although both TRS and TRJS nanocomposites showed comparatively good dispersion in brine up to saturation (30 wt/v% NaCl) and standard API brine by visual inspection as presented in Fig. 7(a), the stability of the dispersions was quantitatively monitored by checking the variation in particle size over 30 days (Fig. 7(b)). Several interesting features or characteristics are presented in Fig. 7(b). As expected, the grafting of PAA@PNVCL on both hemispheres of the particles (TRS) contributed to the larger median diameter (172.5 nm) at initial preparation without salts than TRJS (112.25 nm), whose surface was partially grafted with copolymer and the solutions were slightly transparent (Wu et al., 2015). The medium diameter of the TRJS almost corroborates with the average particle size of the TEM analysis. However, the mean particle size of TRS dramatically reduced to ~130.25 nm in 10 wt/v% NaCl brine largely ascribed to the weakening of electrostatic repulsion force as the electrolyte salts essentially screened the ionic groups of copolymer (Cao et al., 2011). Simultaneously, the corresponding solution became opaque, originating from the salting-out effect in worse solvent quality (which was investigated in the transmittance test). With further increases in ionic strength up to saturation (above 26.10 wt/v% NaCl), TRS shared a similar profile to that of parent nanosilica, as the mean particle size was 306.56 nm due to prominent negative charges screened by salts under high ionic strength, which reduced the electrostatic repulsion forces and ultimately led to gradual flocculation of nanoparticles (Fig. 7(b)). The TRS in standard API brine was not exempted from this phenomenon, as the mean particle size rose (~455 nm) as shown in Fig. 7(b). However, the corresponding solutions indicated no sign of sedimentation for 30 days. The mean particle size of TRJS slightly increased with rising ionic strength, revealing that a fraction of electrolyte ions had also screened the ionic groups on the surface of nanomaterials, which presumably caused the weakening interaction between the nanomaterials. Consequently, the copolymer chain gradually extends, leading to increasing excluded volume of the copolymer, and ultimately enhanced dispersion of nanomaterials as illustrated in Fig. 7(c). The mean particle size in 30 wt/v% NaCl brine and API brine for 30 days were detected as ~ 202.18 and ~175.42 nm, respectively. This type of behaviour that improves rather than deteriorates the functions of nanomaterials resembles that of polyampholytes, where the anti-electrolytic effect is observed under increasing ionic strength. Comparatively, the mean particle size in brine was bigger than in API brine largely due to the stronger binding tendency of monovalent to carboxylate ions.

In order to introduce addressable nanocomposites into the petroleum industry, the long-term stability of nanocomposites in brine was also investigated with respect to temperatures. As shown in Fig. 7(d), the mean particle size markedly varied as the temperature increased from 30 to 190 °C. TRS maintained relative stability from 30 to 110 °C and slightly increased to 195.35 nm at 150 °C. TRJS shared the same pattern as that of TRS from 30 to 110 °C and rose to 149.34 nm (at 150 °C). Surprisingly, further increasing to 190 °C suddenly increased the mean particle size of TRS and TRJS by almost 55.78% and 54.23%, respectively, at 190 °C, which could be connected to the gradual deterioration of the grafted chains at high temperatures for 24 h and a strong tendency of particles to flocculate, causing an increase in the particle size under the investigated conditions. Hosseini et al. (2022) and Sadrolhosseini et al. (2017) also observed this phenomenon. The coexistence of salinity and elevated temperature exacerbated the degradation of grafted copolymer chains as the mean particle size (TRS) further increased by 64.34% and 72.52% in brine and API brine, respectively whereas TRJS was by 44.25% and 62.82% under the same conditions, reflecting a reduction in a particle size increase of 31.25% and 13.38% in saturated brine and API brine, respectively. The relative stabilization of TRJS was presumably connected to the anti-polyelectrolyte effect (as explained in the introduction), where the electrolyte ions expanded the residual copolymer film. The preceding findings revealed that TRJS exhibited better long-term stability than TRS in brine, which could be particularly interesting to enhance the stabilization of shale in WBDFs under vigorous conditions.

3.5. Inhibition performance assessment

3.5.1. Linear swelling experiment

The impact of nanomaterials dispersed in distilled water and brine on the swelling extent of Na-Mt over time is shown in Fig. 8(a). It was indicated that the Na-Mt in distilled water had the fastest swelling speed and the highest equilibrium swelling volume. The addition of nanomaterials showed different degrees of clay hydration swelling inhibition. SiNP had a lower swelling inhibition capacity, with a linear swelling rate of 61.54%, whereas TRS and TRJS had comparatively similar linear swelling rates (40.34%). Likewise, this result should be related to the chemical structures of the nanomaterials. SiNP with rigid structural features formed a defective sealing layer with numerous cavities among stacked particles over the core surface, prompting a more straightforward solution (Lei et al., 2022). TRS and TRJS were coated with flexible and dense copolymer brushes that could suppress water invasion. A switch to brine decreased the linear swelling rate of Na-Mt by almost 14.34%, which was expected due to the inhibitory effect of NaCl. SiNP also followed a similar pattern, though the inhibitive effect was still limited (56.85%). Likewise, the linear swelling rates of the nanocomposites decreased due to the "salting out" effect in

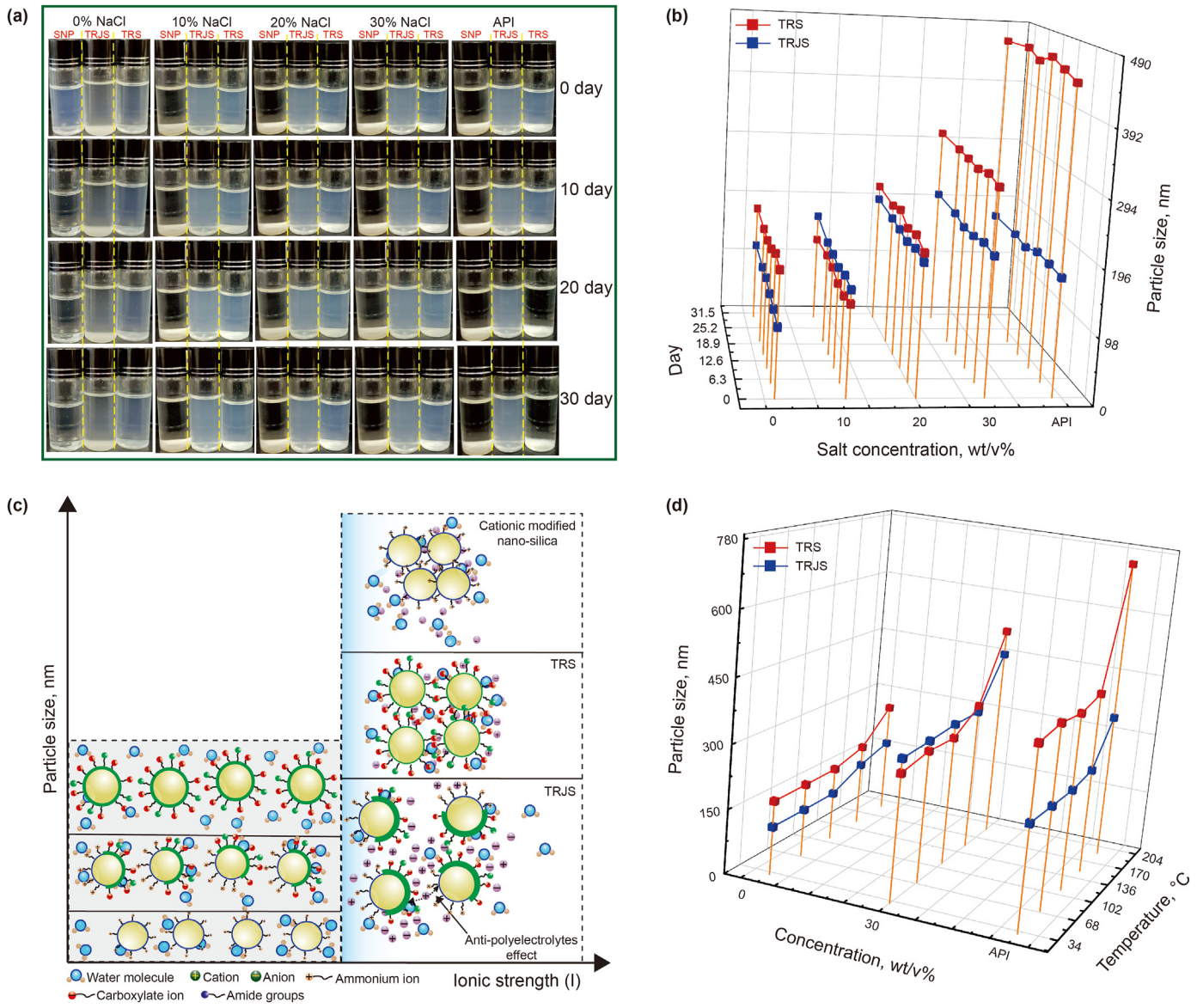

Fig. 7. Colloidal stability of pristine nanosilica and nanocomposites: (**a**) Photographs of nanomaterials dispersion in various brines for 0, 10, 20, and 30 days; (**b**) Mean particle size of nanomaterials in various brines for 0, 10, 20, 30 days; (**c**) Illustration of the responsive colloidal behaviour of nanomaterials as the function of ionic strength (*x*-axis) and particle size (*y*-axis); (**d**) Mean particle size of nanomaterials in various brines as the function of temperature.

the nanocomposites driving formation of a certain hydrophobic layer (i.e., salt-induced hydrophobic interaction which was examined in the transmittance test) over the Mt surface. Comparatively, TRJS produced a much lower linear swelling rate (36.25%) than TRS (38.46%). These results could be attributed to the fact that the counter ions screened the electrostatic attractive force in-between the charged groups in TRJS resulting in a certain level of molecular chains stretching and subsequently increasing colloidal stability of nanomaterials (i.e., anti-polyelectrolytes effect). Thus, this was beneficial for both brush copolymer and ammonium groups at the outward and inward hemispheres, respectively, to strongly interact with clay particles (which was precisely examined in the isotherm adsorption experiment) and thus effectively controlled the swelling behaviour of Na-Mt. Contrarily, the polyelectrolyte effect in TRS contributed to the copolymer shell shrinkage in the presence of electrolyte salts because the counter ions shield the electrostatic repulsion and, led to gradually destabilize the colloidal stability of nanomaterials. As a consequence, TRS had a reinforced hydrophobicity, resulting in minimizing to some extent the interaction with the hydrophilic surface of shale. Thus, a slight increment in the linear swelling behaviour of shale.

When the temperature increased, a number of interesting observations were made. First, the linear swelling increased speedily in distilled water and reached a rate of 69.56%, ascribed to the extensive hydration of Na-Mt, which promoted a more straightforward water invasion. The same phenomenon was responsible for the rising swelling rate (64.23%) with SiNP. Second, for TRS, the swelling speed relatively slowed down, driving a reduced swelling rate from 42.01% to 37.23% at 70 °C. TRJS almost shared the same profile as TRS, as the swelling rate also decreased from 41.25% to 35.97% under the same conditions. The preceding phenomenon could be connected to the construction of a hydrophobic membrane over the surface of the shale above the LCST, which thus, minimized clay particle-free water interaction. Although, TRJS showed slightly superior efficiency than TRS because of the ammonium ion in the inward hemisphere of TRJS, thus favouring

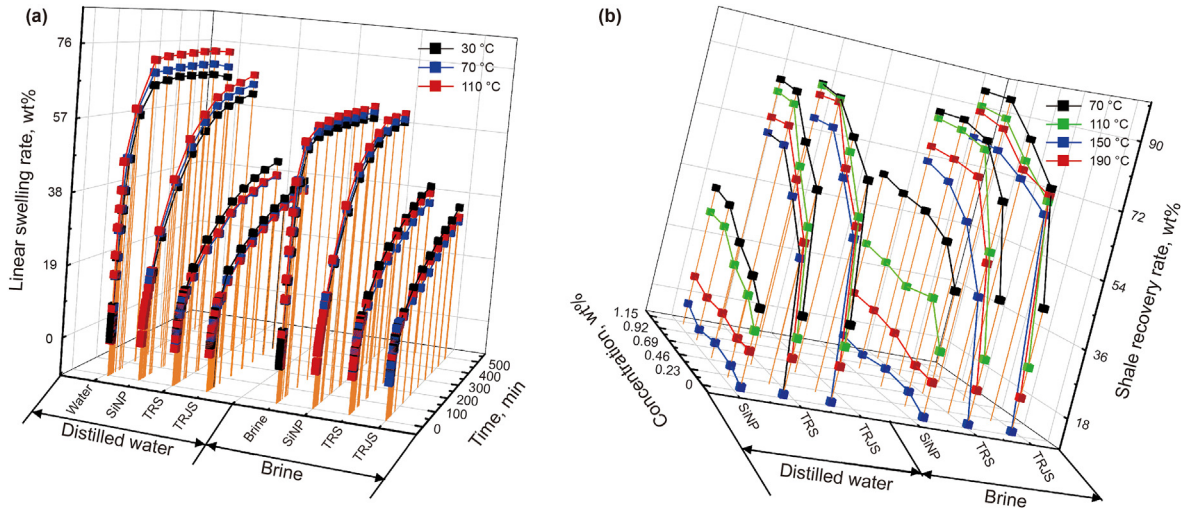

Fig. 8. Chemical inhibitive properties of pristine nanosilica and nanocomposites in brine (4 wt/v%): (**a**) linear swelling test (C_p = 0.2 wt/v%); (**b**) shale cuttings hot-rolling recovery tests.

some interaction with negatively charged sites of Na-Mt particles. This contributed to a slightly better inhibitory effect. Further increasing to 110 °C did not significantly affect their linear swelling rates, as indicated in Fig. 8(a). When switching from distilled water to brine, the linear swelling rate of Na-Mt in brine and SiNP increased due to limited inhibitive effects under the experimental conditions. For nanocomposites, the linear swelling rate of TRS was 35.13% at 70 °C and 32.25% for TRJS above the LCST. As the testing temperature increases to 110 °C, the swelling rate of TRS rose to 39.45%, presumably due to the extensive hydrophobic association phenomenon under the coexistence of high temperature and salinity. This reinforced the polyelectrolyte effect in TRS (as explained in the introduction) driving the formation of a strong hydrophobic and evenly membrane, which could weakly interact with the hydrophilic surface of shale, thus yielding a relatively limited shale hydration inhibitive effect. TRJS endowed with anti-polyelectrolytes effect (as explained in the introduction) reduced the swelling rate to 27.34% because of the nanocomposite molecular chain stretching, which beneficially promoted an effective interaction between ammonium groups in the inward hemisphere and negatively charged sites of clay particles (Boul et al., 2017). Thus, consolidating the formed hydrophobic membrane over the shale surface at high temperatures eventually promoted a better shale hydration inhibition capacity than TRS and other conventional shale inhibitors.

3.5.2. Hot-rolling recovery experiment

The hot-rolling recovery experiment was performed in both distilled water and brine to compare the inhibition performance of nanomaterials using highly reactive shale cuttings after the hot-rolling process from 70 to 190 °C for 16 h as presented in Fig. 8(b). As can be seen, the recovery rate of shale cuttings in pure water was <30.5% throughout the studied temperatures, indicating a potentially significant tendency of shale-cuttings for hydration and dispersion. However, the addition induced a distinctive tendency to suppress the disintegration of shale cuttings. When the concentration of nanomaterials was fixed at 0.2 wt/v%, SiNP slightly increased the shale recovery rate from 30.5% to 38.5%, whereas that of TRN and TRJN rose to 61% and 65.5%, respectively, after oven treatment at a temperature of 70 °C for 16 h, demonstrating different inhibition profiles. With a rising concentration in nanomaterials up to a plateau at 0.8 wt/v%, TRJS yielded a shale recovery rate of 84.5%, whilst those pertaining to TRS and SiNP achieved 82.5% and 48.5%, under the same conditions, respectively. Continuing to increase the concentration of nanomaterials to 1.1 wt/v% had a minor effect on the recovery rate. SiNP showed a limited shale dispersion inhibitive effect, which was also observed in the previous work (Boul et al., 2017). Compared to TRS, the introduction of amino groups in the inward hemisphere of TRJS slightly improved the interaction with clay particles, which resulted in better shale hydration and dispersion inhibitive capacity. When switched to brine, SiNP still demonstrated a limited inhibitive effect, which was expected as ionic strength induces particle flocculation (Boul et al., 2017). Due to the polyelectrolyte effect in TRS (as explained in the introduction) dispersed in poorer water quality, the hydrophobic association phenomenon was reinforced causing a weak interaction with clay particles and eventually a minor effect on the cutting recovery rate (increased by only 3.1%). On the contrary, the cuttings recovery rate of TRJS increased by 11.17% due to the anti-polyelectrolyte effect (as explained in the introduction).

When the hot-rolling temperature was raised up to 190 °C, the recovery rate in distilled water dropped to 13.5%, owing to the extensive disintegration of shale cuttings under vigorous conditions. The addition of SiNP showed a minor effect on the shale recovery rate, even with a further increase in concentration to 1.1 wt/v%. For both TRS and TRJS, the shale recovery rate rose proportionally with nanocomposite concentrations, though the inhibition performance was reduced compared to that of the linear swelling rate. This reducing inhibitory effect could be attributed to the buildup of significant air pressure trapped in the pore space of shale when immersed in the fluids (testing fluids) as a consequence to literally blow shale cuttings apart (disintegration) in the temperature range of 70–110 °C (van Oort et al., 2016). In addition to this effect, the gradual deterioration of the molecular shells of nanocomposites (which was examined early in the DLS experiment), especially at 150 and 190 °C also contributed to reducing the inhibitory effect. However, the cuttings recovery rates of TRS and TRJS were still as high as 68.23% and 71.67%, respectively. The effect of SiNP dispersed in brine on cuttings recovery rate was negligible because it had a nearly identical profile to that of distilled water. Similarly, TRS marginally improved the shale recovery rate by 1.4% due to the polyelectrolyte effect in TRS (as explained in the introduction) at 190 °C. On the contrary, the shale recovery rate of TRJS

improved by 6.63% under the same conditions because of the anti-polyelectrolyte effect in TRJS (as explained in the introduction). TRJS showed slightly comparable shale hydration and dispersion inhibitive capacity to that of TRS in distilled water, but TRJS's anti-polyelectrolyte effect in brine conferred a better inhibitory performance for shale exploitation under vigorous underground conditions.

Generally, TRJS with Janus characteristic is hydrophilic below the LCST, thus, in addition to carboxylate and carbonyl groups in the outward hemisphere, the amino groups in the inward hemisphere, which are converted into ammonium groups favoured strong interaction with clay particles below the LCST due to the anti-polyelectrolyte effect in TRJS (as explained in the introduction). Once the temperature exceeds the LCST of TRJS, the hydrophobic membrane at the outward hemisphere of TRJS was established over the surface of the shale while the ammonium groups (in the inward hemisphere) maintain strong interaction with the hydrophilic shale surface contributing to tightening the hydrophobic membrane over the shale surface for better shale hydration inhibition capacity.

3.5.3. Plugging performance experiment

Controlling the pressure transmission into the shaly underground is an indicator of plugging efficiency (Ewy and Morton, 2009). As presented in Fig. 9, the fluid pressure penetration rose rapidly from 1 to 2 MPa over 6 h for brine. Once interacting with dispersions of nanocomposites, the fluid pressure penetration reduced gradually to 1.90 MPa after 13 h for TRS, whereas that of TRJS attained 1.87 MPa after 15 h at ambient temperature (below the LCST of the nanocomposites). TRJS not only exhibited greater fluid pressure penetration but also a much longer time than TRS. With TRJS having not only a smaller average particle size than TRS (as demonstrated by the DLS analysis) but also an inward hemisphere grafted with amino groups, the particles could fit and be trapped into a much greater number of nano- and micro-pore structures, resulting in a more effective plugging effect. When testing above the LCST value (70 °C) of nanocomposites, the fluid pressure penetration decreased to 1.30 MPa, which was attributed to the formation of a hydrophobic membrane over the shale surface to prevent water ingress into the shale formation. However, as the temperature increased to 150 °C, the fluid pressure penetration rose to 1.37 MPa. TRJS shared a dissimilar profile compared to TRS as the fluid pressure penetration reduced to 1.21 MPa and remained virtually constant as the temperature increased to 150 °C. In contrast to TRJS, TRS resulted in a larger wetting angle due to the polyelectrolyte effect in TRS (which was examined in the later wettability test), which contributed to the construction of a loose hydrophobic membrane over the shale surface as a consequence of slight incremental fluid pressure penetration under these conditions. Wang et al. (2017) observed a similar phenomenon. The colloidal stability of TRJS which was governed by the anti-polyelectrolyte effect (as explained in the introduction) enabled the ammonium ion at the inward hemisphere to create nano-plugging into the internal multi-scale pore structure of shale leading to consolidation of the hydrophobic membrane of the outward hemisphere over the shale surface. Thus, the establishment of a tight hydrophobic membrane over the shale surface was beneficial to better control the fluid pressure penetration. The findings indicated that TRJS had better plugging capacity than TRS when investigated under the same conditions.

The data of the shale permeability test obtained from the bottom pressure building up confirmed the observed phenomenon. The change in permeability of the same shale samples with respect to nanocomposites at a fixed temperature was tracked as a key to reflect the plugging efficiency. The permeability of the shale core was obtained as 7.05×10^{-7} Darcy, and reduced to 2.63×10^{-7}, and 2.33×10^{-7} Darcy after interacting with the TRS and TRJS at 30 °C, respectively. For TRN tested at elevated temperatures, the permeability first diminished from 2.63×10^{-7} to 0.075×10^{-7} Darcy at 70 °C, and increased to 0.098×10^{-7} Darcy at 150 °C, whereas for TRJS, the permeability significantly reduced from 2.33×10^{-7} to 0.055×10^{-7} Darcy as the temperature increased from 30 to 150 °C. Although both TRS and TRJS could act as excellent physical plugging agents, TRJS demonstrated a better capacity to control fluid pressure penetration.

3.6. Interaction between the nanocomposites and clay particles

3.6.1. Electrophoretic mobility (EPM) analysis

Studies have shown that the adsorption of materials on sodium montmorillonite (Na-Mt) surface, which strongly relies on pH value of the environments, can increase the electrical potential of Na-Mt thereby raising the hydration shell thickness of Na-Mt particles through electrostatic stabilization which enhances the dispersion of Mt particles (Cao et al., 2017). The EPM of nanocomposites dispersed in distilled water at distinct pH is shown in Fig. 10(a). TRJS produced a low and nearly constant negative surface charge with increasing pH, which could be attributed to the conversion of amino groups hemisphere into ammonium ions under acidic conditions. This reduced the negative signal of carboxylate ions when tested at pH $\geq$ 7. Schmid et al. also came across similar pH dependence for stimuli-responsive zwitterion microgels (Schmid et al., 2015). On the contrary, the EPM of TRS was higher due to

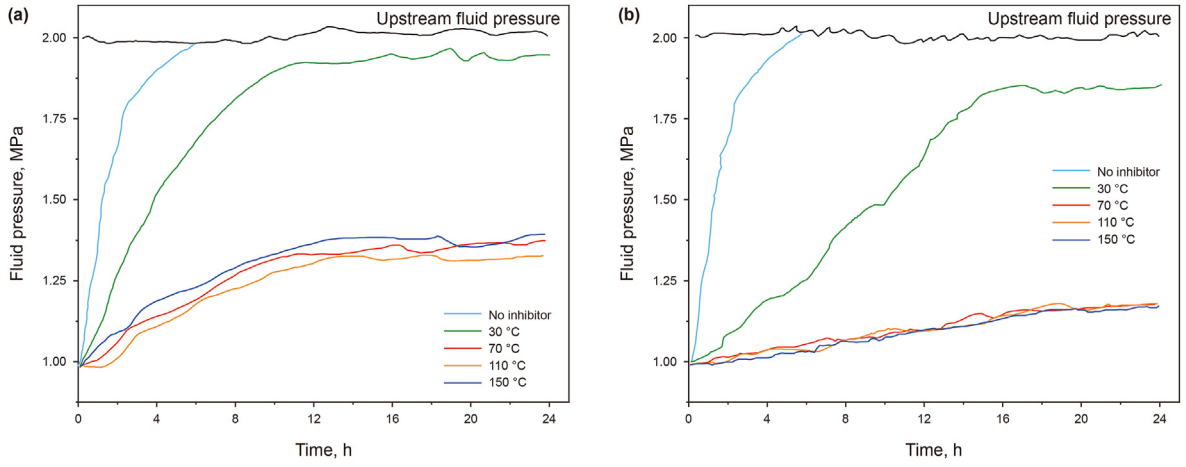

Fig. 9. Physical plugging properties of nanocomposites. Note: (**a**) TRS, and (**b**) TRJS.

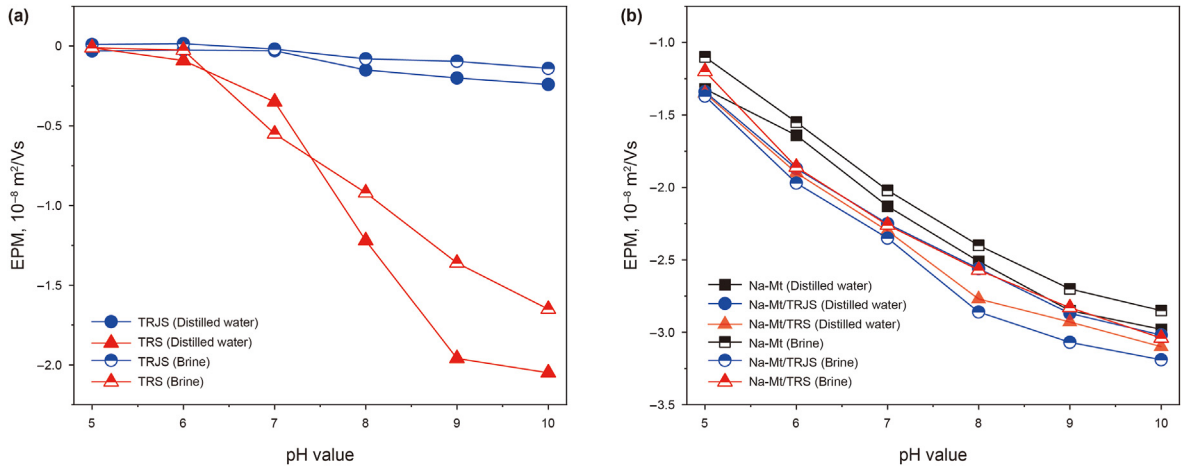

Fig. 10. EPM of nanocomposites at different pH value. Note: (**a**) Nanocomposites without Na–Mt; (**b**) Nanocomposites with Na-Mt.

the conversion of acid carboxylic groups into carboxylate groups with rising pH, which resulted in a highly negative value of EPM. The EPM of nanocomposites in brine presented in the same plot indicated that TRJS was positively charged in the pH ranging from 5 to 7, and marginally reduced with further increasing pH to 10 (negatively charged) which was attributed to the anti-polyelectrolyte effect (as explained in the introduction). Comparatively, the EPM of TRS significantly diminished in the whole range of pH largely ascribed to the polyelectrolyte-effect (as explained in the introduction) (Grzadka and Chibowski, 2009). As shown in Fig. 10(b), the rise in EPM of Na-Mt is in line with the charge of smectites due to the isomorphic substitution (Anderson and Bertsch, 1993). When the nanocomposites were incorporated into Mt dispersed in distilled water, the EPM increased, which was indicative of the more dispersed state of the Mt particles. This was credited to the screening effect of the edge charges of Mt platelets with anionic groups in nanocomposites, causing the electrostatic repulsion between the colloids (Ma et al., 2019). The EPM of TRS was slightly greater than that of TRJS, especially above the pH value of 8, which indicated better dispersion stability for TRS under the studied conditions. The same plot indicated the EPM of the system in brine with respect to pH value. The degree of variation in the EPM of Mt can be described by the double layer theory, which reveals that exposure to electrolyte salts suppresses the thickness of the electric double layer (Zadaka et al., 2010). Additionally, with increasing pH values from 5 to 10, the EPM of Na-Mt/TRS varied from -1.2×10^{-8} to -3.04×10^{-8} m^2/Vs which was consistent with the results in Fig. 10(a), whereas that of TRJS was from -1.37×10^{-8} to $-3.19 \times 10^{\times 8}$ m^2/Vs, which indicated a higher adsorption capacity of TRJS onto Mt (which was examined later in the isothermal absorption experiment), even better than in distilled water. This may be explained by the anti-polyelectrolyte effect in TRJS (as explained in the introduction), which was beneficial for the adsorption of ammonium groups in the inward hemisphere of TRJS on the negatively charged sites of Na-Mt driving better dispersion stability under the studied conditions. The findings of the pH-responsive experiment highlight the contributions of the amino groups' hemisphere (i.e., deprotonation/protonation), which promoted stronger interaction with Mt particles, and ultimately could promote a better stabilization of clays in water-based drilling fluids.

3.6.2. Surface wettability assessment

The wettability of shale-pellets was studied through investigation of the contact angle between the surface of the shale and the

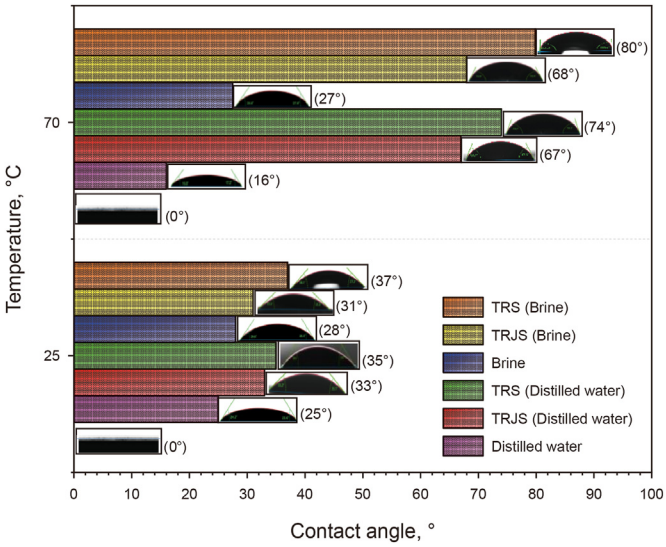

Fig. 11. Contact angle of shale after contacted nanocomposites dispersion at different temperatures.

nanocomposites dispersed in both water and brine below and above the LCST, as indicated in Fig. 11. As noticed, the contact angle of the untreated shale surface was zero. This value was recorded as 25° for distilled water, suggesting that the shale surface showed water-wet characteristics under these conditions. The exposure of the shale surface to nanocomposite dispersions slightly reduced the hydrophilicity of the shale surface. However, TRJS demonstrated a slightly stronger affinity with the surface of shale (33°) compared to TRS (35°) due to the protonated amino groups (ammonium ions) hemisphere of nanomaterials (TRJS), which induced a certain interaction with clay particles, resulting in a reduction of the hydrophobicity of the system. When switching from distilled water to brine, the contact angle increased to 28° for brine, indicating a reduced affinity with the shale surface, which was expected for NaCl as it exhibits a certain inhibitory effect (Siddiqui et al., 2019). The contact angle of TRS in brine was measured at 37°, which was higher than that in distilled water (35°) due to the polyelectrolyte effect (as explained in the introduction) in TRS. In comparison with TRS, the contact angle of TRJS diminished to 31°, probably attributed to the anti-polyelectrolytes effect (as explained in the introduction) in TRJS, where the electrolyte

salts shielding effect contributed to stretching the TRJS molecular chains in brine. Additionally, the presence of ammonium ions, carboxylate, and amide groups may interact with clay particles to increase the affinity for the shale surface.

When heated above the LCST value in distilled water, both TRJS and TRS dispersions prominently reduced the affinity with shale surfaces, and the wettability switched from a strongly water-wet to a moderately water-wet characteristic due to the temperature-induced-hydrophobic association of thermo-responsive subunits in nanocomposites (Xiao et al., 2018a). Nevertheless, TRJS still showed a stronger affinity with the shale surface in distilled water and even marginally varied in brine than that of TRS, as displayed in Fig. 11 presumably attributed to the anti-polyelectrolyte effect (as explained in the introduction) of TRJS, which contributed to mitigate the excessive temperature-induced hydrophobic association. The preceding trends in the responsive behaviour of nanocomposites were consistent with those of the transmittance tests presented in Fig. 6. These findings validated our previous hypothesis that TRJS strongly interacted with the negatively charged sites of clay particles via the ammonium groups in the inward hemisphere, which contributed to enhancing its affinity with shale surfaces under the coexistence of heat and salinity compared to TRS. Thus, driving the establishment of a tight hydrophobic membrane over the shale surface, which would be beneficial to effectively mitigate water ingress in the shale formation.

3.6.3. X-ray diffraction (XRD) analysis

Based on the above results of the shale surface wettability test, the nanocomposites (TRJS and TRS) can interact with clay particles, which minimized the contact with water depending upon the geometry of particles and the environmental conditions. Thereby, the XRD analysis was adopted to precisely follow the contribution of the geometry of the nanocomposites on variation of interlayer spacing of Na-Mt with respect to environmental conditions as shown in Fig. 12. According to Fig. 12(a), the interlayer spacing of Na-Mt was 15.35 Å at 25 °C in distilled water. After interacting with nanocomposites, this value rose to 16.81 Å in the case of TRJS, whereas that of TRS produced an interlayer spacing of 17.62 Å, which was indicative of the successful intercalation of the nanocomposites into the interlayer spacing of Na-Mt (Huang et al., 2021a). From the preceding findings, it was obvious that the intercalation of TRS contributed to a larger interlayer spacing than TRJS ascribed to the higher M_w of the grafted copolymer on the surface of nanomaterial. The interlayer spacing of Na-Mt reduced to 15.19 Å upon heating at 70 °C, mainly credited to the evaporation of water molecules (Dong et al., 2019). The nanocomposites\Na-Mt systems were not exempted from this effect, as shown in Fig. 12(a). However, their interlayer spacings were still higher than that of Na-Mt, largely ascribed to the transfer from hydrophilicity to the hydrophobicity of the thermo-responsive nanocomposites as the system was heated above the LCST. As a result, the free water was ejected from the interlayer spacings, mainly due to the formation of hydrophobic mono-layer arrangements under these conditions.

When switching from distilled water to brine, the low affinity of sodium to cation exchange marginally affected the interlayer spacing, whereas TRJS produced a larger interlayer spacing, followed by TRS in brine as indicated in Fig. 12(b). This propensity of TRJS to enlarge the interlayer spacing was presumably connected to its better hydration capability due to the anti-polyelectrolyte effect in TRJS (as explained in the introduction), which was consistent with the data of colloidal stability analysis. TRJS shared the same profile as that of room temperature when the solutions were heated to 70 °C. Their results were consistent with the results of contact angle measurements, confirming that the ammonium ion in the inward hemisphere of TRJS induced a certain driving force with clay particles, which was further improved in brine as a result to favour strong interaction with negatively charged sites of clay particles. This prevented the alteration of the shale surface from water-wet to strong oil-wet, which beneficially exerted a prominent effect in stabilizing the interlayer spacings. Thereby, effectively suppressing the swelling and dispersion of shale.

3.7. SEM analysis

The SEM photographs of the surface micro-morphology of the shale core after the plugging test and air-dried reveal interesting characteristics. Firstly, the control sample (shale without inhibitor) showed large cavities and micro-fractures along the bending plane from where water could ingress into the formation (Fig. 13(a)). Secondly, after being exposed to nano-fluid samples, the shale's surface was compacted because the nanocomposites could plug the macro- and micro-fractures in the shale revealing thermo-adaptiveness. The preceding phenomenon favourably induced the formation of a hydrophobic shield at elevated temperature, which minimized the contact angle between shale and water resulting in preserving the integrity of the shale block as presented in Fig. 13(b).

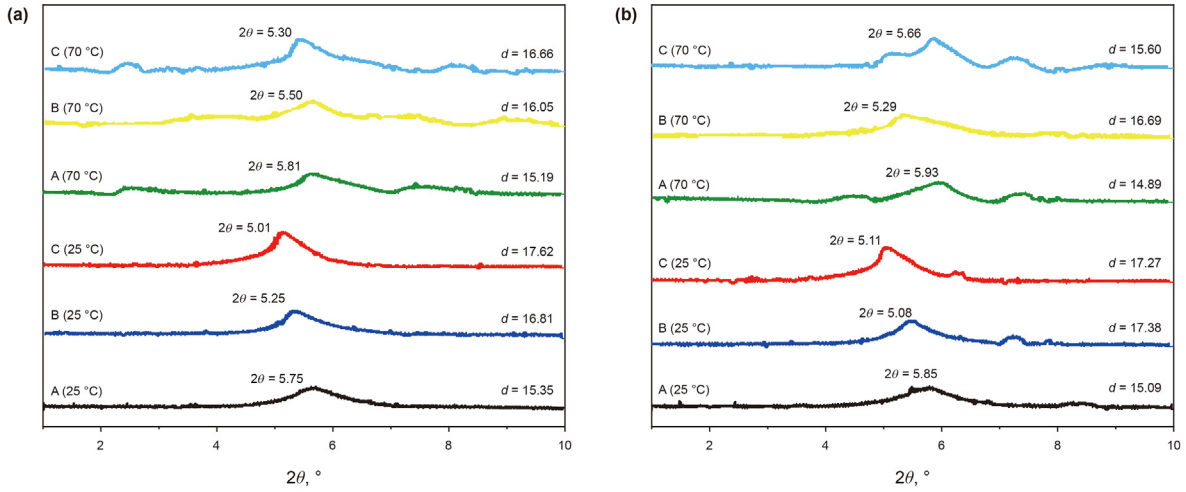

Fig. 12. Influence of nanocomposites adsorption on the swelling of Na-Mt upon warming: (**a**) X-ray diffraction patterns of Na-Mt in distilled water, (**b**) X-ray diffraction patterns of Na-Mt in brine. Na-Mt (A); Na-Mt/TRJS (B); Na-Mt/TRS (C).

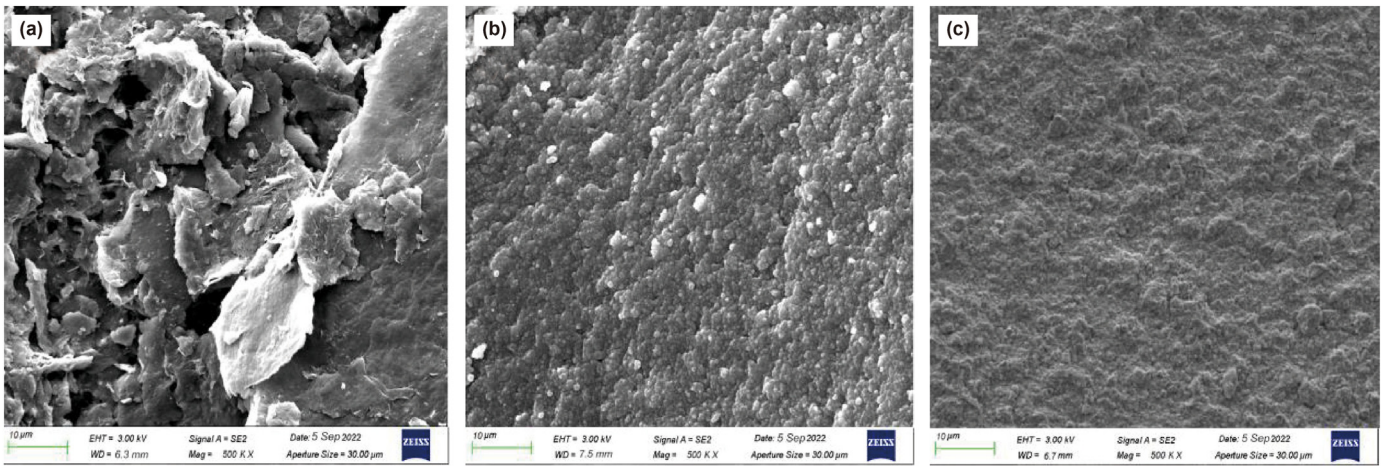

Fig. 13. SEM micro-photographs of shale core end face after plugging test: (**a**) Brine; (**b**) shale sample interaction with TRS; (**c**) shale sample interaction with TRJS.

Thirdly, contrary to the previous scenario, the surface micro-morphology of the shale core treated with TRJS was smothered and the grains were more compact, presumably ascribed to a stronger interaction with the internal structure of shale (Fig. 13(c)). The amino groups in the inward hemisphere of nanosilica could be converted into ammonium ions, which afforded a strong interaction with the surface charged of shale. Thus, the establishment of a tight hydrophobic layer would be favoured under a driving force to effectively oppose fluid pressure penetration under vigorous conditions.

3.8. Adsorption characteristics

We further attempted to elucidate the adsorption mechanism of the shale stabilizers. For this purpose, the Dubinin-Radushkevich (D-R) isotherm model was employed to characterize the nature of sorption and adsorption capacities of TRJS and TRS as shown in Fig. 14 (Hu and Zhang, 2019). The exponential form of the equation is given as follows;

$$q_e = q_{max}\exp\left(-K_{DR}\varepsilon^2\right) = q_{max}\exp\left[-K_{DR}\left(RT\ln\left(1+\frac{1}{C_e}\right)\right)^2\right] \tag{8}$$

The linearized form can be written as;

$$\ln q_e = \ln q_{max} - K_{DR}\left[RT\left(1+\frac{1}{C_e}\right)\right]^2 \tag{9}$$

where q_e represents the adsorbed adsorbate quantity per unit mass of adsorbent at equilibrium in mg/g; q_{max} represents the maximal theoretical adsorption capacity in mg/g; K_{DR} represents the Dubinin-Radushkevich constant in mol^2/kJ^2, which depends on the mean free energy change (E); ϵ represents the adsorption potential in kJ/mol.

The free energy change (E) is given as follows;

$$E = \frac{1}{(2K_{DR})^{1/2}} \tag{10}$$

C_e represents the concentration at equilibrium in mol/L, R represents the universal gas constant (8.314×10^{-3} kJ/mol/K), and T is the absolute temperature °K.

Both constants q_{max} and K_{DR} in the D-R equation were obtained from the intercept and slope of the linear line, respectively.

Table 3 indicates the D-R isotherm equation parameters and correlation coefficients. The D-R isotherm model well fitted the experimental data based on a strong correlation coefficient obtained throughout, translating its suitability to describe the adsorption nature of TRJS and TRS under the studied conditions. As the temperature rose, the q_{max} diminished, which could be plausibly due to weak interaction with Na-Mt platelets. As a matter of fact, the hydrophilic character of nanocomposites surfaces progressively turned into a hydrophobic one above the LCST, which contributed to reducing the adsorption capacity of nanocomposites. However, in comparison with TRS, TRJS yielded higher values throughout, which translated its stronger adsorption capacity and the higher possibility to be firmly trapped into the interstice of Na-Mt. The same table reveals that the surface energies of adsorption for both nanocomposites were heterogeneous, which was reflected by an unstable adsorption potential, especially in the case of TRS. As the temperature rose from 30 to 90 °C, the interaction between TRS and clay particles was controlled by a physical process as indicated by the mean free energy (E) (E>8 kJ/mol) (Hu and Zhang, 2019). For TRJS, the E>8 kJ/mol throughout, revealing the fundamental characteristics of chemisorption as indicated in Table 3.

It was evident that the presence of protonated amino groups inward hemisphere of TRJS enhanced the adsorption capacity, which was beneficial to create a charge balance. The coexistence of chemisorption and physical adsorption may have contributed to maximizing the adsorption capacity, and eventually the mean free adsorption energy. The optimal adsorption of TRJS and TRS onto Na-Mt was detected at pH=8 and their adsorption capacity gradually diminished with further increasing from 8 to 10. The reduced adsorption capacity may be credited to repulsion forces between the net negatively charged sites of clay particles and both carboxylate ions of AA subunits and isolated silanolate groups at the surface of nanosilica at a high pH as shown in Fig. 14(c) (Huang et al., 2015). The adsorption of both TRJS and TRS with respect to NaCl concentrations was also examined and the results are presented in Fig. 14(d). As observed, the adsorption capacity of TRJS was higher and marginally varied with rising brine concentrations presumably credited to the anti-polyelectrolyte effect (as explained in the introduction), whereas TRS experienced a large decrease in adsorption capacity. Such a decrease in adsorption capacity was due to high ionic strength, which led to the screening effect of functional groups onto the surface of nanomaterials because of particle agglomeration and ultimately compromised their

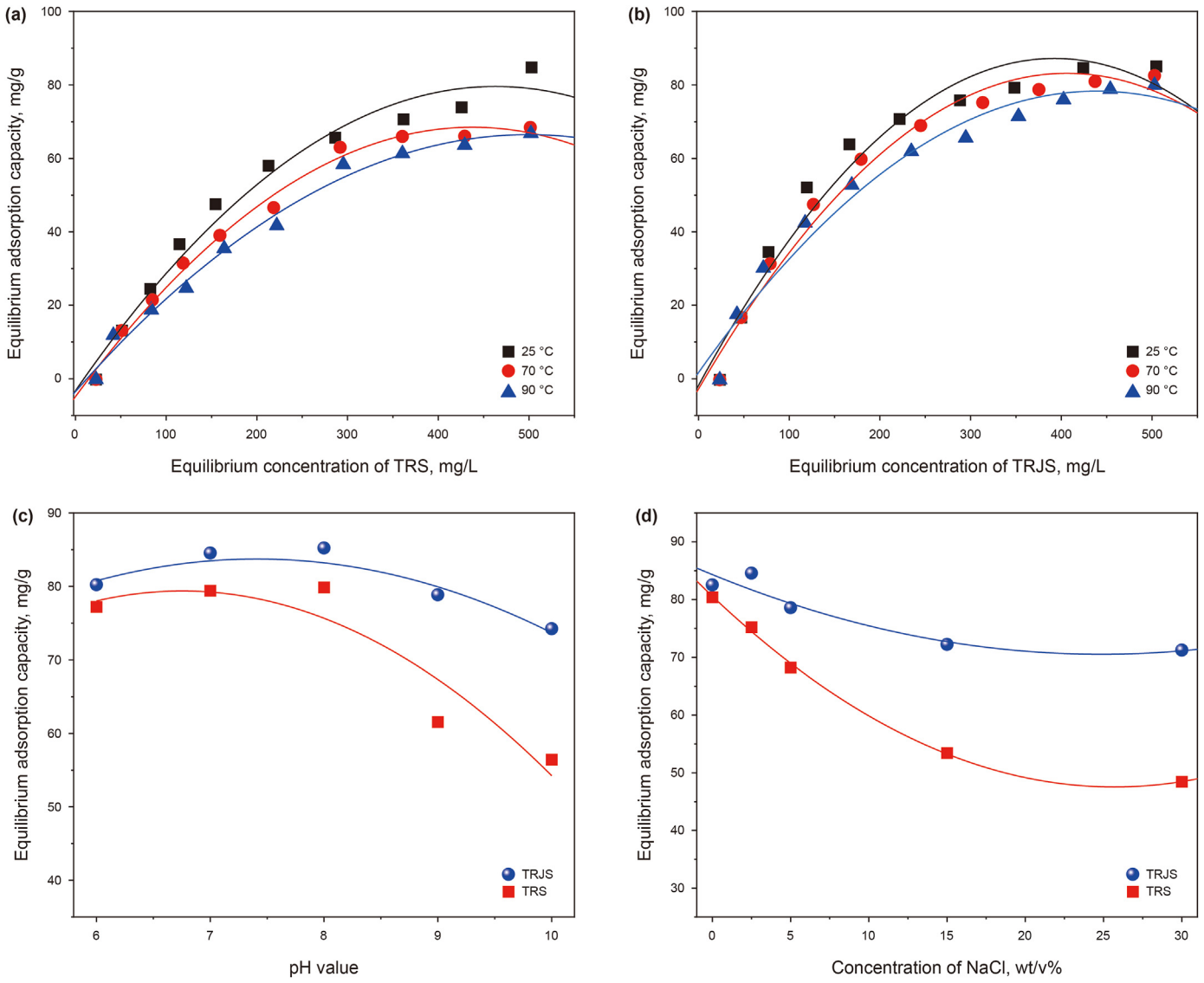

Fig. 14. Adsorption isotherm of TRJS and TRS on Na-Mt. Note: (**a** and **b**) effect of temperature; (**c**) effect of pH value; (**d**) effect of NaCl concentration.

Table 3
Parameters of D-R isotherm for TRJS and TRS on Na–Mt at different temperatures.

Samples	Temperature, °C	q_{max}	$K_{DR}\times10^{-3}$	E	R^2
TRJS	30	18.76	4.85	10.15	0.98
	70	16.28	4.98	10.02	0.98
	90	15.07	4.24	10.85	0.98
TRS	30	12.85	4.78	10.22	0.93
	70	8.18	7.96	7.92	0.92
	90	6.24	8.45	7.69	0.94

attachment to the surface of clay particles.

3.9. Potential shale stabilization mechanism

A potential mechanism for shale stabilization with TRJS is illustrated in Fig. 15. Clay consists of a number of platelets with permanently negatively charged surfaces and edges, and its electrical properties depend on pH conditions. In an acidic environment, the edge (Al–OH_2^+) of clay platelets becomes positively charged, while in neutral pH condition, it is electrically neutral (Al–OH) and switched to Al–O^- at a high pH (Jin et al., 2019; Luckham and Rossi, 1999; Tombácz and Szekeres, 2004). As the octahedral Al sheet is exposed, the edge of clay platelets is positively charged. TRJS showed a certain level of anti-polyelectrolyte effect (as explained in the introduction), in which sodium chloride ions shielded the electrostatic attraction forces between TRJS, prompting improved dispersion of nanomaterials in brine. It is speculated that ammonium ions in the inward hemisphere and the carboxylate groups in the outward hemisphere would first adsorb onto the negatively charged sites and Al^+ on the edge of the clay platelets via chemisorption. While the amide groups tend to interact with Al–OH via hydrogen bonding. These interactions can prompt the intercalation of TRJS into interlayer spacing of clay particles, resulting in the formation of hydrophobic mono-layer arrangements under a certain level of salt-induced hydrophobic association phenomenon in the presence of salts, which efficiently expelled water from the interlayer spacing, an indication of inhibitory effect. In addition to the strong interaction with clay particles, TRJS with small particle size (as evidenced in DLS analysis) not only fit into the pores but also could be trapped into the multi-scale pore structures to obstruct fluid pressure transmission.

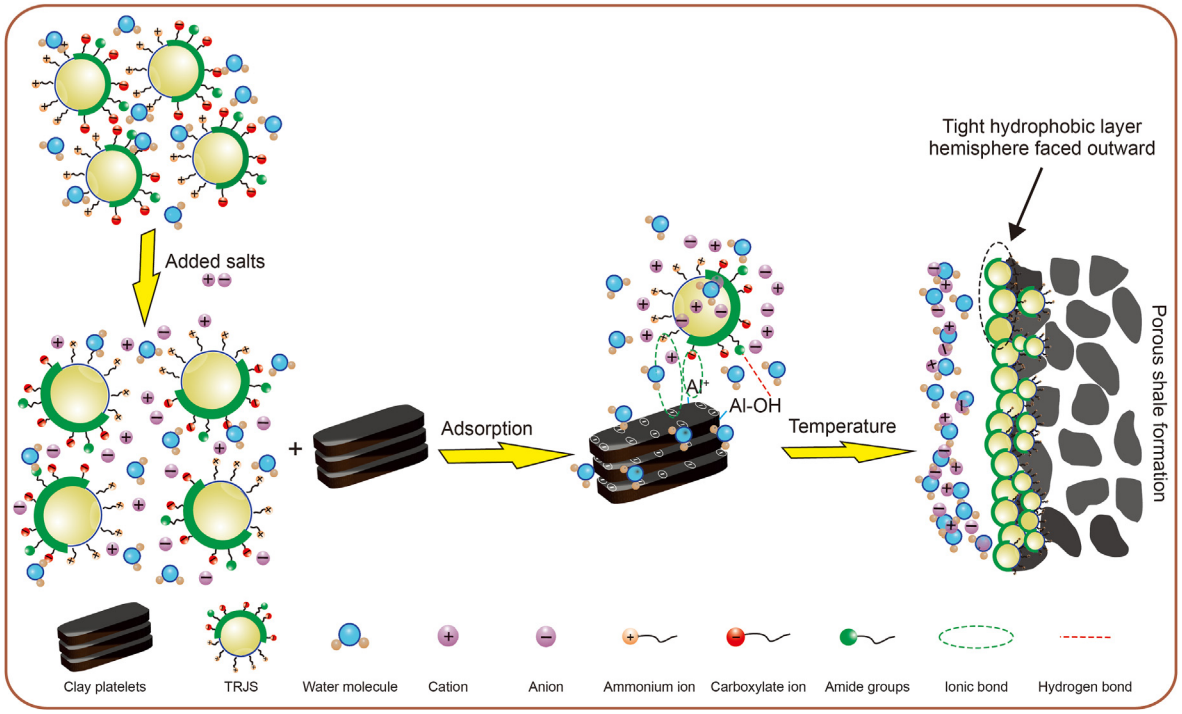

Fig. 15. Proposed mechanism of shale stabilization with TRJS.

When heated above the LCST of TRJS, the self-association of the thermo-responsive shield hemisphere, which induced the formation of a hydrophobic membrane over the shale surface significantly minimized the shale-water interactions. Additionally, as TRJS particles could fit and be trapped into much more nano/micro-pores structures, they also exhibit thermo-responsive self-adaptiveness characteristic into the multi-scale structure of the shale driven by particle swelling to effectively plug the shale formation at high temperatures, which was beneficial to impede drilling fluid ingress into the shale formation (Akhtarmanesh et al., 2013; Cai et al., 2012). The anti-polyelectrolyte effect of TRJS in brine (as explained in the introduction) permitted an effective synergistic effect between the adsorption properties and thermo-responsive characteristics promoted the establishment of a tight hydrophobic layer over the shale surface in brine under geothermal conditions. This eventually reduced the interaction between the water and shale. The favourable dispersion stability of TRJS in brine beneficially improved not only the plugging performance but also efficiently controlled the permeability of the shale, as shown in the above pore pressure penetration experiment. TRJS could prominently suppress the hydration and dispersion of the shale matrix and eventually minimized formation damage (Gao et al., 2016).

3.10. Compatibility test

The effect of TRJS on key parameters of the BF was also examined and the results are compiled in Table 4. The increment in *PV* with the increasing TRJS concentrations in drilling fluid samples could be connected to rising flow frictions between liquid-liquid, solid-liquid, and solid-solid layers (Xie et al., 2018). The increase in *PV* also portrayed a strong interaction between the nanocomposites (TRJS) and clay particles (which was observed in the EPM analysis). Simultaneously, the ratio of *YP*/*PV* shared the same pattern as that of *PV*, which indicated a better capability of TRJS to improve the pseudoplastic behaviour, which is believed to rise the viscosity in the annular space, thus more conducive to the drilling fluid cleaning efficiency of the wellbore by displacing drilled cuttings from the drill path during drilling operations (Oseh et al., 2019; Ricky et al., 2022). Furthermore, as TRJS concentration increased from 0 to 1.1 wt/v%, FL_{API} decreased and could be as low as 5.0 mL, indicating TRJS's ability to control WBDF filtrate loss. Simultaneously, the density remained unchanged at 0.2 wt/v% but rose to 2.12 g/cm^3 from 0.5 to 1.1 wt/v%, which was due to additional solid particle accumulation with a rising concentration in the fluid samples.

Table 4
Effect of TRJS on the performance of the BF.

Formula	Test conditions	*AV*, mPa·s	*PV*, mPa·s	*YP*, Pa	*YP*/*PV*	*ρ*, g/cm^3	FL_{API}, mL	FL_{HTHP}, mL
BF	BHR	85	55	30.5	0.55	2.00	5.9	–
BF+0.2% TRJS	BHR	87.5	56.5	31.5	0.55	2.00	5.7	–
BF+0.5% TRJS	BHR	88	57	32	0.56	2.10	5.4	–
BF+0.8% TRJS	BHR	89.5	58	33.5	0.57	2.12	5.2	–
BF+1.1% TRJS	BHR	90.5	59.5	35	0.58	2.13	5.0	–
BF	AHR	62.5	50	12	0.24	2.00	10.8	27.3
BF+1.1% TRJS	AHR	65	51	13.5	0.26	2.05	9.1	26.5

Note: FL_{HTHP} was conducted at 190 °C; BHR: Before hot-rolling; AHR: After hot-rolling.

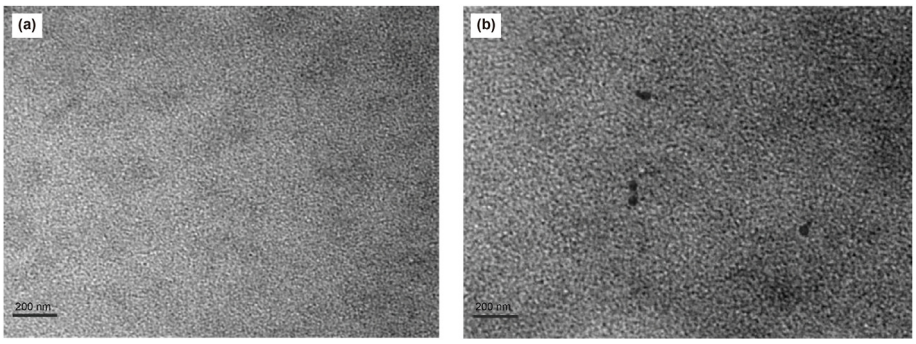

Fig. 16. TEM micro-photographs of filtration loss fluid: Note: (**a**) filtration loss of BF; (**b**) filtration loss of BF bearing TRJS.

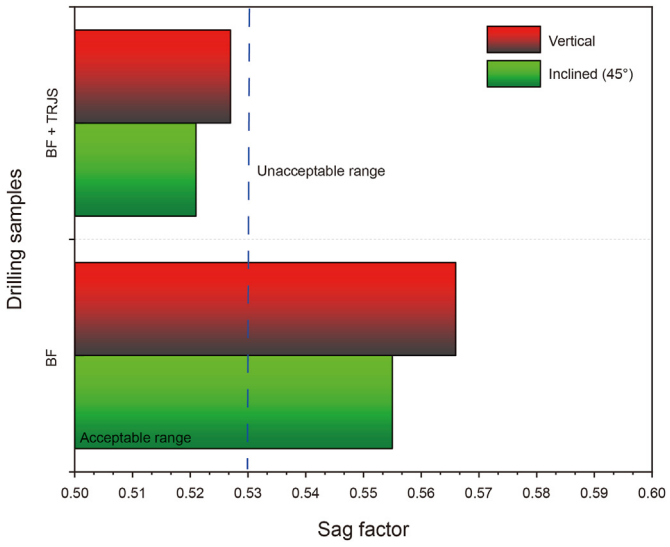

Fig. 17. Static sag tendency of drilling fluid samples AHR.

The oven-treatment process was designed to assess the thermo-stability of nanocomposites bearing drilling fluid. As indicated in Tables 4 and it was observed that TRJS showed a minor effect on the rheological controlling capability of the fluid sample, according to the *AV*, *PV*, *YP*, and the ratio of *YP*/*PV*. The same observation was made for the filtration loss controlling capability of the fluid sample, which was maintained within reasonable ranges without significant impact on filtration loss properties and density AHR.

Besides, the TEM micro-photographs in Fig. 16 revealed the presence of certain particles (ranging from 60 to 155 nm with average particle size of 88 nm) in the filtration fluid (Fig. 16(b)) to achieve the expected shale inhibitory effect under realistic conditions. Moreover, the data related to the sagging tendency of the drilling fluid samples taken under vertical and inclined (45°) conditions under static conditions for 24 h were calculated based on the density from top and bottom fluid samples using the following relationship (Mohamed et al., 2020).

$$\text{Sag factor} = \frac{\text{bottom desnsity}}{\text{bottom density} + \text{top density}} \tag{11}$$

As indicated in Fig. 17, for vertical and inclined sections, the sag factors of BF-bearing TRJS were 0.521 and 0.527, respectively. These values were within an acceptable range of 0.50–0.53 reported in the literature (Alabdullatif et al., 2014; Maxey et al., 2007), whereas the sagging phenomenon is anticipated for BF as the sag factor was higher than 0.53. Thus, TRJS exhibited not only a certain tendency to mitigate the sagging phenomenon but also a thermo-stability in WBDF at 190 °C.

4. Conclusions

A novel responsive stabilized Janus nanosilica (TRJS) was successfully prepared to improve the plugging efficiency in WBDFs for drilling troublesome shale formations. Compared to SiNP and TRS, TRJS demonstrated favourable salt-tolerance in saturated brine and standard API brine over 30 days at ambient temperature and better thermo-stability at 190 °C for 24 h based on the anti-polyelectrolyte effect. According to both linear swelling and hot-rolling shale dispersion experiments, 0.2 wt/v% of TRJS in pure water and brine yielded a linear swelling rate of 34.26% and 27.34% at 110 °C, respectively. Shale recovery rates at the concentration of 1.1 wt/v% TRJS in pure water and brine were 71.67% and 79.3% at 190 °C, respectively. Comparatively, SiNP and TRS showed limited chemical inhibition under the same conditions. Benefiting from the improved chemical inhibition, TRJS consistently controlled the fluid pressure penetration above the LCST throughout the investigated temperatures. The ammonium ions in the inward hemisphere as well as the carboxylate ion and amide groups could spontaneously interact with clay platelets via chemisorption and hydrogen bonds with significant interactions in brine. As a result, TRJS was firmly trapped into the interlayer confinement of clay while simultaneously expelling water molecules. Thus, a tight hydrophobic layer could form from the outward hemisphere of TRJS, which better inhibited shale-water interactions compared to TRS. TRJS exhibiting a wavering wettability characteristic was particularly advantageous as its imbued improved chemical inhibition and physical plugging simultaneously via an effective synergistic in brine.

For attractive characteristic of TRJS in drilling practice, it is recommended to maintain the pH of the fluid under an alkaline environment (preferentially around pH = 8) to ensure a stronger interaction between amino groups' hemispheres with Na-Mt platelets, for better stabilization of clays particles. Moreover, the addition of certain amounts of salts in the drilling fluid is also necessary to drive the expected anti-polyelectrolyte effect while the formation temperature (at a temperature higher than the LCST value) is essential to induce the establishment of a tight hydrophobic layer from the outward hemisphere of the particle over the shale surface. Thus, TRJS could therefore find potential application prospects as high-performance shale stabilizers in WBDFs for the exploitation of shale under vigorous environments.

CRediT authorship contribution statement

Alain Pierre Tchameni: Data curation, Formal analysis, Funding acquisition, Methodology, Writing – original draft,

Conceptualization. **Lv-Yan Zhuo:** Validation, Writing – review & editing. **Lesly Dasilva Wandji Djouonkep:** Investigation, Visualization, Writing – review & editing. **Robert Dery Nagre:** Investigation, Visualization, Writing – review & editing. **Lu-Xin Chen:** Data curation, Investigation, Visualization. **Lin Zhao:** Project administration, Resources, Validation. **Chao Ma:** Project administration, Validation, Writing – review & editing. **Bin-Qiang Xie:** Project administration, Supervision, Validation, Writing – review & editing.

Declaration of competing interest

The authors declare that they have no known competing financial interests or personal relationships that could have appeared to influence the work reported in this paper.

Acknowledgments

This work was financially supported by the National Natural Science Foundation of China (Grant No.52150410427), the Key Support Program for Foreign Experts of the Ministry of Science and Technology of the People's Republic of China (No.wgxz2022057) and funding for post-doctoral work by the Department of Human Resources and Social Security of Hubei Province.

Nomenclatures

A	Cross-section area of the shale core samples
AA	Acrylic acid
AEAPTS	N-β-(Aminoethyl)-γ-aminopropyl trimethoxy silane
AHR	After hot-rolling
AIBI	2,2-azobis (2-methylpropionamide) dihydrochloride
API	American petroleum institute
AV	Apparent viscosity
2-BIBB	2-bromoisobutyryl bromide
β	Static compression ratio of testing fluids
BF	Base-fluid
BHR	Before hot-rolling
C_0	Nanocomposites concentration before adsorption onto Na-Mt
C_1	Nanocomposites concentration after adsorption onto Na-Mt
CNPC	China National Petroleum Corporation
DMF	Dimethylformamide
DLS	Dynamic light scattering
ϵ	Adsorption potential
E	Mean free energy change
EPM	Electrophoretic mobilities
EtOH	Ethanol
FT-IR	Fourier transform infrared resonance
GPC	Gel permeation chromatography
H_0	Initial thickness
HTHP	High-temperature high pressure
K	Permeability of the shale core samples
K_{DR}	Dubinin-Radushkevich constant
D	Linear swelling rate
L	Length of shale core samples
LCST	Lower critical solution temperature
m	Weight of Na-Mt
μ	Viscosity of testing fluids
M_w	Molecular weight
Na-Mt	Sodium montmorillonite
NH_2-SiO_2	Amino-functionalized nanosilica
NH_2-SiO_2/wax	Amino-functionalized nanosilica/wax beads
NH_2-SiO_2-Br	ATRP-initiator immobilized onto amino-functionalized nanosilica
NPA	SiO_2-g-poly(NIPAm-*co*-AMPS) (Amino-based- SiO_2)
NVCL	N-Vinylcaprolactam
OBDFs	Oil-based drilling fluids
ρ	*Density*
PAA@PNVCL	Poly(acrylic acid-*co*- N-vinylcaprolactam)
PDI	Molecular distribution
P_m	Upstream pressure
PMDETA	N, N, N, N, N″-pentamethyldiethylenetriamin
P_o	Pore pressure
P(L,t)	Real-time downstream pressure
PV	Plastic viscosity
M	Weight of adsorbed nanocomposites
q_e	Adsorbed adsorbate quantity of per unit mass of adsorbent at equilibrium
q_{max}	Maximal theoretical adsorption capacity
R_i	Initial reading
R_t	Reading after the appointed time t
R	Shale recovery rate
SBDFs	Synthetic-based drilling fluids
SD-SEAL	Poly(MMA-*co*-St)-*g*-poly(NIPAm-*co*-AA)
SEM	Scanning electron microscope
SI-ATRP	Surface-initiated atom transfer radical polymerization
SiNP	Pristine nanosilica
SiNP-PAA@PNVCL	Copolymer for symmetric modified nano-silica
SMP-3	Sulfonated phenolic resin-3
SPNH	Sulfonated lignite
V	Volume of solution
V	Enclosed volume of the testing fluids in the downstream
t	Overall experimental time
TEA	Trimethylamine
TEM	Transmission electron microscope
TGA	Thermogravimetry analysis
TRJS	Thermo-responsive Janus nanosilica (NH_2-SiNP-PAA@PNVCL)
TRS	Symmetrical thermo-responsive nanosilica (SiNP-PAA@PNVCL)
VIS-H	Polymeric viscosifier
W_2	Weight of shale cuttings recovered after oven-treatment
WBDFs	Water-based drilling fluids
XRD	X-ray diffraction
YP	Yield point

References

Abbas, M.A., Zamir, A., Elraies, K.A., Mahmood, S.M., Rasool, M.H., 2021. A critical parametric review of polymers as shale inhibitors in water-based drilling fluids. J. Petrol. Sci. Eng. 204, 108745. https://doi.org/10.1016/j.petrol.2021.108745.

Akhtarmanesh, S., Shahrabi, M.J.A., Atashnezhad, A., 2013. Improvement of wellbore stability in shale using nanoparticles. J. Petrol. Sci. Eng. 112, 290–295. https://doi.org/10.1016/j.petrol.2013.11.017.

Akimoto, A.M., Ueki, T., Yoshida, R., 2014. Thermoresponsive polymers. In: Kobayashi, S., Müllen, K. (Eds.), Encyclopedia of Polymeric Nanomaterials. Springer, Berlin, Heidelberg. https://doi.org/10.1007/978-3-642-36199-9_169-1.

Alabdullatif, Z.A., Al-Yami, A.S., Wagle, V.B., Bubshait, A.S., Al-Safran, A.M., 2014. Development of New Kill Fluids with Minimum Sagging Problems for High Pressure Jilh Formation in Saudi Arabia. In: Abu Dhabi International Petroleum Exhibition and Conference. https://doi.org/10.2118/171683-ms.

Altum, G., Serpen, U., 2005. Investigating improved rheological and fluid loss performance of sepiolite. In: Proceedings World Geothermal Congress.

Anderson, M.A., Bertsch, P.M., 1993. Electrophoretic mobility and particle size of clay using laser dopper velocimeter –photon correlation spectroscopy. Soil Sci. Soc. Am. J. 57, 1641–1643. https://doi.org/10.2136/sssaj1993.03615995005700060039x.

Bai, X., Yong, Y., Luo, X., Deng, L., Li, K., Zhou, Y., 2022. Synthesis and application of temperature-sensitive polymer as a novel plugging agent for water-based drilling fluids. J. Appl. Polym. Sci. 139, 1–13. https://doi.org/10.1002/app.52524.

Barry, M.M., Jung, Y., Lee, J.K., Phuoc, T.X., Chyu, M.K., 2015. Fluid filtration and rheological properties of nanoparticle additive and intercalated clay hybrid

bentonite drilling fluids. J. Petrol. Sci. Eng. 127, 338–346. https://doi.org/10.1016/j.petrol.2015.01.012.
Boul, P.J., Reddy, B.R., Hillfiger, M., Pete O'Connell, T., Thaemlitz, C., 2017. Functionalized nanosilicas as shale inhibitors in water-based drilling fluids. SPE Drill. Complet. 32, 121–130. https://doi.org/10.2118/185950-pa.
Caenn, R., Chillingar, G.V., 1996. Drilling fluids: state of the art. J. Petrol. Sci. Eng. 14 (3–4), 221–230. https://doi.org/10.1016/0920-4105(95)00051-8.
Cai, J., Chenevert, M.E., Sharma, M.M., Friedheim, J., 2012. Decreasing water invasion into Atoka shale using nonmodified silica nanoparticles. SPE Drill. Complet. 27, 103–112. https://doi.org/10.2118/146979-PA.
Cao, J., Tan, Y., Che, Y., Ma, Q., 2011. Synthesis of copolymer of acrylamide with sodium vinylsulfonate and its thermal stability in solution. J. Polym. Res. 18, 171–178. https://doi.org/10.1007/s10965-010-9404-6.
Cao, J., Meng, L.W., Yang, Y.P., Zhu, Y.J., Wang, X.Q., Yao, C.Y., 2017. Novel acrylamide/2-acrylamide-2-methylpropanesulfonic acid/4-vinylpyridine terpolymer as an anti-calcium contamination fluid-loss additive for water-based drilling fluids. Energy Fuel. 31 (11), 11963. https://doi.org/10.1021/acs.energyfuels.7b02354, 1197.
Cao, X.Q., Shi, Y.W., Li, W.Z., Zeng, P.Y., Zheng, Z., Feng, Y.J., Yin, H.Y., 2021. Comparative studies on hydraulic fracturing fluids for high-temperature and high-salt oil reservoirs: synthetic polymer versus guar gum. ACS Omega 6 (39), 25421–25429. https://doi.org/10.1021/acsomega.1c03394.
De Gennes, P.G., 1992. Soft matter. Sci. 256, 495–497. https://doi.org/10.1126/science.256.5056.495.
Djouonkep, L.D.W., Xie, B., Tao, H., Zhuo, L., Tchameni, A.P., Zhao, L., 2023. Investigating the structure-to-property of thermo-thickening polymers capped by different structural side chains. React. Funct. Polym. 186, 105569. https://doi.org/10.1016/j.reactfunctpolym.2023.105569.
Dong, W., Pu, X., Ren, Y., Zhai, Y., Gao, F., Xie, W., 2019. Thermoresponsive bentonite for water-based drilling fluids. Materials 12, 2115. https://doi.org/10.3390/ma12132115.
Du, W.C., Wang, X.Y., Liu, M., Bi, T.F., Song, S.X., Zhang, J., Chen, G., 2019. Synthesis and performance of AM/SSS/THDAB as clay hydration dispersion inhibitor. Polímeros. 29, 1–7. https://doi.org/10.1590/0104-1428.06519.
Du, W., Slaný, M., Wang, X., Chen, G., Zhang, J., 2020. The inhibition property and mechanism of a novel low molecular weight zwitterionic copolymer for improving wellbore stability. Polymers 12, 708. https://doi.org/10.3390/polym12030708.
Durand, A., Hourdet, D., 1999. Synthesis and thermoassociative properties in aqueous solution of graft copolymers containing poly (N-isopropylacrylamide) side chains. Polymer 40, 4941–4951. https://doi.org/10.1016/S0032-3861(98)00698-3.
Ewy, R.T., Morton, E.K., 2009. Wellbore-stability performance of water-based mud additives. SPE Drill. Complet. 24, 390–397. https://doi.org/10.2118/116139-PA.
Friedheim, J.E., 1997. Second-generation synthetic drilling fluids. J. Petrol. Technol. 49, 724–728. https://doi.org/10.2118/38251-JPT.
Gao, C., Miska, S.Z., Yu, M., Ozbayoglu, E.M., Takach, N.E., 2016. Effective enhancement of wellbore stability in shales with new families of nanoparticles preserving and cutting of shale samples. In: Deepwater Drilling and Completions Conference, pp. 1–12. https://doi.org/10.2118/180330-MS.
Ge, H.K., Yang, L., Shen, Y.H., Ren, K., Meng, F.B., Ji, W.M., Wu, S., 2015. Experimental investigation of shale imbibition capacity and the factors influencing loss of hydraulic fracturing fluids. Petrol. Sci. 12, 636–650. https://doi.org/10.1007/s12182-015-0049-2.
Geng, Y., Sun, J., Wang, J., Wang, R., Yang, J., Wang, Q., Ni, X., 2021. Modified nanopolystyrene as a plugging agent for oil-based drilling fluids applied in shale formation. Energy & Fuels 6, 16543–16552. https://doi.org/10.1021/acs.energyfuels.1c02546.
Grzadka, E., Chibowski, S., 2009. Influence of a kind of electrolyte and its ionic strength on the adsorption and zeta potential of the system: polyacrylic acid/MnO_2/electrolyte solution. Physicochem. Probl. Miner. Process. 43, 31–42. https://www.journalssystem.com/ppmp/Influence-of-a-kind-of-electrolyte-and-its-ionic- strength-on-the-adsorption-and-zeta,79186,0,2.html.
Guo, H., Brûlet, A., Rajamohanan, P.R., Marcellan, A., Sanson, N., Hourdet, D., 2015. Influence of topology of LCST-based graft copolymers on responsive assembling in aqueous media. Polymer 60, 164–175. https://doi.org/10.1016/j.polymer.2015.01.038.
Hong, L., Jiang, S., Granick, S., 2006. Simple method to produce Janus colloidal particles in large quantity. Langmuir 22, 9495–9499. https://doi.org/10.1021/la062716z.
Hosseini, M.S., Khazaei, M., Misaghi, M., Koosheshi, M.H., 2022. Improving the stability of nanofluids via surface-modified titanium dioxide nanoparticles for wettability alteration of oil-wet carbonate reservoirs. Mater. Res. Express 9, 0–13. https://doi.org/10.1088/2053-1591/ac4fdf.
Hu, Q., Zhang, Z., 2019. Application of Dubinin–Radushkevich isotherm model at the solid/solution interface: a theoretical analysis. J. Mol. Liq. 277, 646–648. https://doi.org/10.1016/j.molliq.2019.01.005.
Huang, W., Zhao, C., Qiu, Z., Leong, Y.K., Zhong, H., Cao, J., 2015. Synthesis, characterization and evaluation of a quadripolymer with low molecular weight as a water based drilling fluid viscosity reducer at high temperature (245 °C). Polym. Internal 64, 1352–1360. https://doi.org/10.1002/pi.4923.
Huang, D.C., Xie, G., Peng, N.Y., Zou, J.G., Xu, Y., Deng, M.Y., Du, W.C., Xiao, Y.R., Wang, J.J., Luo, P.Y., 2021a. Synergistic inhibition of polyethylene glycol and potassium chloride in water-based drilling fluids. Petrol. Sci. 18, 827–838. https://doi.org/10.1007/s12182-020-00543-w.
Huang, X. Bin, Sun, J.S., Huang, Y., Yan, B.C., Dong, X.D., Liu, F., Wang, R., 2021b. Laponite: a promising nanomaterial to formulate high-performance water-based drilling fluids. Petrol. Sci. 18, 579–590. https://doi.org/10.1007/s12182-020-00516-z.
Jin, J., Wang, H., Jing, Y., Liu, M., Wang, D., Li, Y., Bao, M., 2019. An efficient and environmental-friendly dispersant based on the synergy of amphiphilic surfactants for oil spill remediation. Chemosphere 215, 241–247. https://doi.org/10.1016/j.chemosphere.2018.09.159.
Kang, Y., Yang, B., Li, X., Yang, J., You, L., Chen, Q., 2017. Quantitative characterization of micro forces in shale hydration and field applications. Petrol. Explor. Dev. 44, 328–335. https://doi.org/10.1016/S1876-3804(17)30038-1.
Koteeswaran, S., Pashin, J.C., Ramsey, J.D., Clark, P.E., 2017. Quantitative characterization of polyacrylamide–shale interaction under various saline conditions. Petrol. Sci. 14, 586–596. https://doi.org/10.1007/s12182-017-0166-1.
Lei, M., Huang, W., Sun, J., Shao, Z., Chen, Z., Chen, W., 2021. Synthesis and characterization of high-temperature self-crosslinking polymer latexes and their application in water-based drilling fluid. Powder Technol. 389, 392–405. https://doi.org/10.1016/j.powtec.2021.05.045.
Lei, M., Huang, W., Sun, J., Jin, Z., Huang, X., 2022. The utilization of self-crosslinkable nanoparticles as high-temperature plugging agent in water-based drilling fluid. SPE J. 27, 2628–2641. https://doi.org/10.2118/209805-PA.
Li, W., Zhao, X., Ji, Y., Peng, H., Chen, B., Liu, L., Han, X., 2016a. Investigation of biodiesel-based drilling fluid, Part 2: formulation design, rheological study, and laboratory evaluation. SPE J. 21, 1767–1781. https://doi.org/10.2118/180926-PA.
Li, W., Zhao, X., Ji, Y., Peng, H., Chen, B., Liu, L., Han, X., 2016b. Investigation of biodiesel-based drilling fluid, Part 1: biodiesel evaluation, invert-emulsion properties, and development of a novel emulsifier package. SPE J. 21, 1755–1766. https://doi.org/10.2118/180918-PA.
Li, X., Xu, Z., Yin, H., Feng, Y., Quan, H., 2017. Comparative studies on enhanced oil recovery: thermoviscosifying polymer versus polyacrylamide. Energy & Fuels 31, 2479–2487. https://doi.org/10.1021/acs.energyfuels.6b02653.
Li, X., Jiang, G., Yang, L., Wang, K., Shi, H., Li, G., Wu, X., 2019a. Application of gelatin quaternary ammonium salt as an environmentally friendly shale inhibitor for water-based drilling fluids. Energy & Fuels 33, 9342–9350. https://doi.org/10.1021/acs.energyfuels.9b01798.
Li, X., Yin, H.Y., Zhang, R.S., Cui, J., Wu, J.W., Feng, Y.J., 2019b. A salt-induced viscosifying smart polymer for fracturing inter-salt shale oil reservoirs. Petrol. Sci. 16, 816–829. https://doi.org/10.1007/s12182-019-0329-3.
Li, X., Wang, Y., Hou, Q., Cai, W., Xu, Y., Zhao, Y., 2021. Fabrication of thermo-responsive Janus silica nanoparticles and the structure–performance relationship in Pickering emulsions. Res. Chem. Intermed. 47, 3899–3917. https://doi.org/10.1007/s11164-021-04486-8.
Liu, X., Wen, Y., Qu, J., Geng, X., Chen, B., Wei, B., Wu, B., Yang, S., Zhang, H., Ni, Y., 2019. Improving salt tolerance and thermal stability of cellulose nanofibrils by grafting modification. Carbohydr. Polym. 211, 257–265. https://doi.org/10.1016/j.carbpol.2019.02.009.
Luckham, P.F., Rossi, S., 1999. Colloidal and rheological properties of bentonite suspensions. Adv. Collold Inter. Sci. 82 (1), 43–92. https://doi.org/10.1016/S0001-8686(99)00005-6.
Lv, K., Huang, P., Zhou, Z., Wei, X., Luo, Q., Huang, Z., Yan, H., Jia, H., 2020. Study of Janus amphiphilic graphene oxide as a high-performance shale inhibitor and its inhibition mechanism. Front. Chem. 8, 1–9. https://doi.org/10.3389/fchem.2020.00201.
Lv, K., Sun, J., Liu, J., 2017. Polymer elastic particle reservoir protection agent and drilling fluid containing the same. U.S. Patent No. 9771509 B1. United States Patent and Trademark Office. https://patents.justia.com/patent/9771509.
Ma, L., Luo, P., He, Y., Zhang, L., Fan, Y., Jiang, Z., 2019. Ultra-stable silica nanoparticles as nano-plugging additive for shale exploitation in harsh environments. Nanomaterials 9, 1683. https://doi.org/10.3390/nano9121683.
Maxey, J., 2007. Rheological analysis of static and dynamic sag in drilling fluids. Annu. Trans. Nord. Rheol. Soc. 15, 181. https://nrs.blob.core.windows.net/pdfs/nrspdf-f3741626-0a14-4902-8c2a-aaa94c73eb68.pdf.
Mehtar, M., Brangetto, M., Abou Soliman, A., Mielke, S., Alfonzo, N., Young, S., 2010. Effective implementation of high performance water based fluid provides superior shale stability offshore Abu Dhabi. In: Abu Dhabi International Petroleum Exhibition and Conference. https://doi.org/10.2118/138564-MS.
Mohamed, A., Al-Afnan, Saad, Elkatatny, S., Hussein, I., 2020. Prevention of barite sag in water-based drilling fluids by a urea-based additive for drilling deep formations. Sustainability 12, 2719. https://doi:10.3390/su12072719.
Naji, A.J., Al-Jelawy, H.M., Saadoon, S.A., Ejel, A.T., 2021. Rehabilitation and strengthening techniques for reinforced concrete columns: review. In: J. Phys.: Conference Series 1895. https://doi.org/10.1088/1742-6596/1895/1/012049.
OECD, 2017. Dispersion stability of nanomaterials in simulated environmental media. In: OECD Guideline for the Testing of Chemicals, pp. 1–4. https://doi.org/10.1787/2074577x.
Oseh, J.O., Mohd Norddin, M.N.A., Ismail, I., Gbadamosi, A.O., Agi, A., Mohammed, H.N., 2019. A novel approach to enhance rheological and filtration properties of water–based mud using polypropylene–silica nanocomposite. J. Petrol. Sci. Eng. 181, 106264. https://doi.org/10.1016/j.petrol.2019.106264.
Parvizi Ghaleh, S., Khodapanah, E., Tabatabaei-Nezhad, S.A., 2020. Experimental evaluation of thiamine as a new clay swelling inhibitor. Petrol. Sci. 17, 1616–1633. https://doi.org/10.1007/s12182-020-00466-6.
Ranka, M., Brown, P., Hatton, T.A., 2015. Responsive stabilization of nanoparticles for extreme salinity and high-temperature reservoir applications. ACS Appl. Mater. Interfaces 7 (35), 19651–19658. https://doi.org/10.1021/acsami.5b04200.

Ren, X., Liu, R., Ma, Z., 2021. Experimental investigation of a low-molecular-weight polymer coating agent for deep-sea oil and gas drilling. J. Pet. Explor. Prod. Technol. 11, 2953–2962. https://doi.org/10.1007/s13202-021-01198-y.

Ricky, E., Mpelwa, M., Wang, C., Hamad, B., Xu, X., 2022. Modified corn starch as an environmentally friendly rheology enhancer and fluid loss reducer for water-based drilling mud. SPE J. 27, 1064–1080. https://doi.org/10.2118/209195-PA.

Rivera-Tarazona, L.K., Campbell, Z.T., Ware, T.H., 2021. Stimuli-responsive engineered living materials. Soft Matter 17, 785–809. https://doi.org/10.1039/D0SM01905D.

Sadrolhosseini, A.R., Abdul Rashid, S., Zakaria, A., 2017. Synthesis of gold nanoparticles dispersed in palm oil using laser ablation technique. J. Nanomater. 2017, 6496390. https://doi.org/10.1155/2017/6496390.

Schmid, A.J., Schroeder, R., Eckert, T., Radulescu, A., Pich, A., Richtering, W., 2015. Synthesis and solution behaviour of stimuli-sensitive zwitterionic microgels. Colloid Polym. Sci. 293, 3305–3318. https://doi.org/10.1007/s00396-015-3749-7.

Shen, Y., Zhu, Y., Gao, Z., Qu, S., Yang, L., Gao, L., He, Q., Lai, N., 2022. Nano-SiO_2 grafted with temperature-sensitive polymer as plugging agent for water-based drilling fluids. Arabian J. Sci. Eng. 48, 9401–9411. https://doi.org/10.1007/s13369-022-07486-x.

Siddiqui, M.A.Q., Chen, X., Iglauer, S., Roshan, H.A., 2019. Multiscale study on shale wettability: spontaneous imbibition versus contact angle. Water Resour. Res. 55 (6), 5012–5032. https://doi.org/10.1029/2019WR024893.

Song, W., Shi, Y.C., Deng, Y.Q., Zhu, X.X., Zhang, Z.Q., Hu, X.G., 2013. Investigation of beat-waves generation with high efficiency. Appl. Phys. Lett. 103 (17), 5–8. https://doi.org/10.1063/1.4826252.

Soto-Cantu, E.I., 2018. Synthesis and Surface Characterization of Silica- Polypeptide Composite Particles. LSU Doctoral Dissertations. 214. https://repository.lsu.edu/gradschool_dissertations/214.

Sun, J., Chang, X., Zhang, F., Bai, Y., Lv, K., Wang, J., Wang, J., 2020. Salt-responsive zwitterionic polymer brush based on modified silica nanoparticles as a fluid-loss additive in water-based drilling fluids. Energy & Fuels 34 (2), 1669–1679. https://doi.org/10.1021/acs.energyfuels.9b04109.

Tchameni, A.P., Xie, B., Liu, W., Li, Y., Zhao, L., Luo, M., 2020a. Amphoteric tetramer as a filtration-loss reducer in low-solid phase water based drilling fluids under high thermal-saline conditions. J. Dispersion Sci. Technol. 42 (6), 920–933. https://doi.org/10.1080/01932691.2020.1721296.

Tchameni, A.P., Xie, B., Zhang, H., Zhao, L., Luo, M., Wen, J., 2020b. Thermo-associating polymers based on cross-linked 2-acrylamido-methylpropane sulfonic acid, part A: synthesis and solution behavior. Colloids Surf., A 124611. https://doi.org/10.1016/j.colsurfa.2020.124611.

Tchameni, A.P., Xie, B., Li, Y., Liu, W., Zhao, L., Luo, M., Wen, J., 2021a. Thermo-associating polymers based on cross-linked 2-acrylamido-methylpropane sulfonic acid, part B: effect of co-solutes on solution behavior. Colloids Surf., A 608, 125531. https://doi.org/10.1016/j.colsurfa.2020.125531.

Tchameni, A.P., Xie, B., Ma, J., Wang, Y., Zhao, L., Xie, L., 2021b. Thermo-associating copolymer based on cross-Linked 2-acrylamido-methylpropane sulfonic acid, part C: experimental study into the performance of deepwater aqueous drilling fluids. Colloids Surf., A 612, 125965. https://doi.org/10.1016/j.colsurfa.2020.125965.

Tombácz, E., Szekeres, M., 2004. Colloidal behavior of aqueous montmorillonite suspensions: The specific role of pH in the presence of indifferent electrolytes. Appl. Clay. Sci. 2775–2794. https://doi.org/10.1016/j.clay.2004.01.001.

van Oort, E., 1997. Physico-chemical stabilization of shales. In: International Symposium on Oilfield Chemistry. https://doi.org/10.2118/37263-MS.

van Oort, E., Hoxha, B.B., Hale, A., Aldin, M., Patterson, R., 2016. How to test fluids for shale compatibility. In: American Association of Drilling Engineers Fluids Technical Conference and Exhibition. AADE-16-FTCE-77.

Wang, W., Qiu, Z., Zhong, H., Huang, W., Zhao, X., Dong, B., Bao, D., 2015. Preparation and properties of thermos-sensitive polymer (NIPAm-co-AA)nano-SiO_2 composite blocking agent for shale gas reservoir. Acta Pet. Sin. 36 (3), 378–384. https://doi.org/10.7623/syxb201503014.

Wang, W., Qiu, Z., Zhong, H., Huang, W., Dai, W., 2017. Thermo-sensitive polymer nanospheres as a smart plugging agent for shale gas drilling operations. Petrol. Sci. 14, 116–125. https://doi.org/10.1007/s12182-016-0140-3.

Wu, H., Yi, W., Chen, Z., Wang, H., Du, Q., 2015. Janus graphene oxide nanosheets prepared via Pickering emulsion template. Carbon 93, 473–483. https://doi.org/10.1016/j.carbon.2015.05.083.

Xiao, S., Ren, B., Huang, L., Shen, M., Zhang, Y., Zhong, M., Yang, J., Zheng, J., 2018a. Salt-responsive zwitterionic polymer brushes with anti-polyelectrolyte property. Curr. Opin. Chem. Eng. 19, 86–93. https://doi.org/10.1016/j.coche.2017.12.008.

Xiao, S., Zhang, Y., Shen, M., Chen, F., Fan, P., Zhong, M., Ren, B., Yang, J., Zheng, J., 2018b. Structural dependence of salt-responsive polyzwitterionic brushes with an anti- polyelectrolyte effect. Langmuir 34, 97–105. https://doi.org/10.1021/acs.langmuir.7b03667.

Xie, G., Luo, P., Deng, M., 2016. A novel method for determining the degree of clay swelling in clay-polymer-water systems. Chem. Technol. Fuels Oils 52 (5), 542–549. https://doi.org/10.1007/s10553-016-0741-y.

Xie, B., Tchameni, A.P., Luo, M., Wen, J., 2021. A novel thermo-associating polymer as rheological control additive for bentonite drilling fluid in deep offshore drilling. Materials Letters 284, 128914. https://doi.org/10.1016/j.matlet.2020.128914.

Xie, B., Ting, L., Zhang, Y., Liu, C., 2018. Rheological properties of bentonite-free water- based drilling fluids with novel polymer viscosifier. J. Petrol. Sci. Eng. 164, 302–310. https://doi.org/10.1016/j.petrol.2018.01.074.

Xie, B., Zhang, X., Li, Y., Liu, W., Luo, M., 2019. Application a novel thermo-sensitive copolymer as a potential rheological modifier for deepwater water-based drilling fluids. Colloids Surf., A 581, 123848. https://doi.org/10.1016/j.colsurfa.2019.123848.

Xiong, Z., Tao, S., Li, X., Shan, W., Dong, H., 2014. Development and application of anti- collapse & anti-drag agent for drilling fluid. Procedia Eng. 73, 55–62. https://doi.org/10.1016/j.proeng.2014.06.170.

Xu, J.G., Qiu, Z., Zhao, X., Huang, W., 2017. Hydrophobic modified polymer-based silica nanocomposite for improving shale stability in water-based drilling fluids. J. Petrol. Sci. Eng. 153, 325–330. https://doi.org/10.1016/j.petrol.2017.04.013.

Xu, J.G., Qiu, Z., Zhao, X., Zhang, Y., Li, G., Huang, W., 2018. Application of nano-polymer emulsion for inhibiting shale self-Imbibition in water-based drilling fluids. J. Surfactants Deterg. 21 (1), 155–164. https://doi.org/10.1002/jsde.12019.

Xu, C., Yang, X., Liu, C., Kang, Y., Bai, Y., You, Z., 2022. Dynamic fracture widthprediction for lost circulation control and formation damage prevention in ultra-deep fractured tight reservoir. Fuel 307, 121770. https://doi.org/10.1016/j.fuel.2021.121770.

Yeap, S.P., 2018. Permanent agglomerates in powdered nanoparticles: formation and future prospects. Powder Technol. 323, 51–59. https://doi.org/10.1016/j.powtec.2017.09.042.

You, L., Kang, Y., Chen, Z., Chen, Q., Yang, B., 2014. Wellbore instability in shale gas wells drilled by oil-based fluids. Int. J. Rock Mech. Min. Sci. 72, 294–299. https://doi.org/10.1016/j.ijrmms.2014.08.017.

Zadaka, D., Radian, A., Mishael, Y.G., 2010. Applying zeta potential measurements to characterize the adsorption on montmorillonite of organic cations as monomers, micelles, or polymers. J. Colloid Interface Sci. 352, 171–177. https://doi.org/10.1016/j.jcis.2010.08.010.

Zhang, T., Li, T.Q., Liu, Y.C., Li, Yang, Guo, G.W., Cui, J.C., Zhou, F.S., 2017. Preparation and rheological properties of attapulgite gel for aqueous suspensions. Adv. Comput. Sci. Res. 59. https://download.atlantis-press.com/article/25870643.pdf.

Zhong, H., Gao, X., Zhang, X., Qiu, Z., Zhao, C., Zhang, X., Jin, J., 2020. Improving the shale stability with nano-silica grafted with hyperbranched polyethyleneimine in water-based drilling fluid. J. Nat. Gas Sci. Eng. 83, 103624. https://doi.org/10.1016/j.jngse.2020.103624.

Zuniga, C.A., Goods, J.B., Cox, J.R., Swager, T.M., 2016. Long-term high-temperature stability of functionalized graphene oxide nanoplatelets in Arab-D and API brine. ACS Appl. Mater. Interfaces 8 (3), 1780–1785. https://doi.org/10.1021/acsami.5b09656.